

The Dark Matter Distribution in the Central Regions of Galaxy Clusters: Implications for CDM

David J. Sand, Tommaso Treu^{1,2}, Graham P. Smith & Richard S. Ellis

California Institute of Technology, Astronomy, mailcode 105-24, Pasadena, CA 91125

djs@astro.caltech.edu

ABSTRACT

We have undertaken a spectroscopic survey of gravitational arcs in a carefully chosen sample of six clusters each containing a dominant brightest cluster galaxy. We use these systems to study the relative distributions of dark and baryonic material in the central regions. Three clusters present both radial and tangential arcs and provide particularly strong constraints on the mass profiles, whereas the other three display only tangential arcs and act as a control set. Following Sand et al. (2002), we analyze stellar velocity dispersion data for the brightest cluster galaxies in conjunction with the arc redshifts and lens models to constrain the dark and baryonic mass profiles jointly. For the systems containing radial arcs we find that the inner dark matter density profile is consistent with a 3-D distribution, $\rho_{DM} \propto r^{-\beta}$, with logarithmic slope $\langle\beta\rangle = 0.52_{-0.05}^{+0.05}$ (68% CL). Similarly, we find that the tangential arc sample gives an upper limit, $\beta < 0.57$ (99% CL). Taking the 6 clusters together, the mean dark matter distribution is inconsistent with the standard Navarro, Frenk & White (1997) value, $\beta=1.0$, at $>99\%$ confidence. In addition, we find considerable cosmic scatter in the β ($\Delta\beta \sim 0.3$) values of the radial arc sample. We find no evidence that systems with radial arcs preferentially yield flatter dark matter profiles as might be expected if they were a biased subset. We discuss the validity of our 1-D mass reconstruction method and verify its conclusions by comparing with results of a more rigorous ray-tracing code that does not assume axial symmetry. Our results extend and considerably strengthen the earlier conclusions presented by Sand et al. (2002) and suggest the relationship between dark and visible matter in the cores of clusters is much more complex than anticipated from recent simulations.

¹Hubble Fellow

²Current Address: Department of Physics & Astronomy, UCLA, Box 951547, Los Angeles, CA 90095-1547

Subject headings: gravitational lensing – galaxies:formation – dark matter – galaxies: elliptical and lenticular, cD

1. Introduction

The cold dark matter (CDM) paradigm has been extremely successful in explaining observations of the universe on large scales at various epochs, from that of the cosmic microwave background, through high redshift studies of the $Ly\alpha$ forest to the distribution of galaxies and clusters in local surveys (e.g. Percival et al. 2001, Spergel et al. 2003; Croft et al. 2002; Bahcall et al. 2003). A primary tool for making the necessary predictions is that of N-body simulations which are now able to resolve structures on highly non-linear scales so that the properties of dark matter (DM) halos can be predicted on \sim kpc scales.

A central prediction arising from CDM simulations is that the density profile of DM halos is universal in form across a wide range of mass scales from dwarf galaxies to clusters of galaxies (e.g. Navarro, Frenk & White 1997; hereafter NFW97). Within a scale radius, r_{sc} , the DM density asymptotes to $\rho \propto r^{-\beta}$ while external to r_{sc} , $\rho \propto r^{-3}$. The value of the logarithmic inner slope, β , is still a matter of debate. However, in nearly all studies, β ranges between 1 (NFW97) and 1.5 (Moore et al. 1998; Ghigna et al. 2000; hereafter referred to as the “Moore” slope for convenience). Recent work by Power et al. (2003) and Fukushige et al. (2003) has suggested that with proper account of the timestep, force accuracy and particle number, the inner slope does not converge to a power law, as predicted from lower resolution simulations, but instead becomes progressively shallow at smaller radii. Power et al. found $\beta=1.2$ at their innermost reliable location. Further work in this area will allow for even more precise predictions of the form of DM halos.

An observational verification of the NFW97 (or Moore) form, via a convincing measurement of β and its scatter over various mass scales, has proved controversial despite the motivation that it offers a powerful test of the CDM paradigm. A major observational hurdle is the importance of convincingly separating the baryonic and non-baryonic components. Indeed, observations may guide the interpretation of the numerical simulations, both because the inclusion of baryons into simulations is difficult (e.g. Frenk 2002) and because it is expensive computationally to simulate a sufficient number of halos (with proper convergence) to characterize the expected scatter in halo shapes.

Most of the observational effort has been directed via dynamical studies of low surface brightness and dwarf galaxies as these are thought to be DM dominated at all radii. How-

ever, analyses of the various datasets have given conflicting values of β and many of the assumptions used have been questioned (see discussion by Simon et al. 2003 and Swaters et al. 2003). Some studies have provided evidence for cores of roughly constant density (e.g. de Blok et al. 2001; de Blok & Bosma 2002; Simon et al. 2003) whereas others find their data are consistent with $\beta=1$ (e.g. van den Bosch & Swaters 2001; Swaters et al. 2003). Steep inner profiles with $\beta \approx 1.5$ seem to be ruled out.

In order to test the simulations convincingly, observations should not be confined to mass scales probed by dwarf galaxies. Accordingly, several attempts have been made to constrain the DM profiles of more massive systems. Observations of spiral and early-type galaxies tend to favor inner slopes that are shallower than predicted by CDM simulations (Treu & Koopmans 2002; Koopmans & Treu 2003; Borriello & Salucci 2002; Borriello, Salucci, & Danese 2003; Jimenez, Verde & Oh 2003), although the dominance of stellar mass at small scales makes it difficult to achieve an accurate measurement of the dark halo component.

More effort has been devoted to galaxy cluster mass scales. Most common has been the use of X-ray observations of the hot intracluster medium under the assumption of hydrostatic equilibrium. Whether hydrostatic equilibrium is maintained in the inner regions, where there are often irregularities and “cooling flows”, remains an important question (see Arabadjis, Bautz & Arabadjis 2003). Within the context of the hydrostatic equilibrium assumption, many studies have considered only a limited range of DM profiles, comparing, for example, NFW (or Moore) fits with those of a non-singular isothermal sphere (e.g. Schmidt, Allen, & Fabian 2001; Allen, Schmidt, & Fabian 2002; Pratt & Arnaud 2002). In general, X-ray analyses have led to wide ranging results, with β ranging from $\simeq 0.6$ (Ettori et al. 2002) through $\simeq 1.2$ (Lewis, Buote & Stocke 2003) to $\simeq 1.9$ (Arabadjis, Bautz & Garmire 2002). However, when using just X-ray data alone, it is difficult to account for the stellar mass of a central brightest cluster galaxy (BCG), which leads to complications in interpreting the shape of the DM density profile at small radii (Lewis et al. 2003). In fact, although the stellar component is small in terms of the total mass of the system, it can dominate the mass density at small radii, and can mimic a cuspy DM halo if it is not taken into proper account.

Gravitational lensing offers a particularly promising probe of the total mass profile. Projected mass maps of the inner regions of clusters constrained by strongly lensed features of known redshift have been compared with CDM predictions (Tyson, Kochanski, & Dell’Antonio 1998, Smith et al. 2001; hereafter S01). By using weak lensing, and stacking a sample of clusters, Dahle, Hannestad, & Sommer-Larsen (2003) found an inner DM slope roughly in agreement with CDM predictions (albeit with large uncertainties). Recently a combined strong and weak lensing analysis of Cl0024 has confirmed the prediction of CDM

numerical simulations that the DM density profile falls off like $\rho \propto r^{-3}$ at large radii, strongly ruling out a density profile that falls off like an isothermal mass distribution (Kneib et al. 2003). A combined strong and weak lensing analysis has also been used to constrain the inner DM slope in the cluster MS2137-23 (Gavazzi et al. 2003; hereafter G03), although the precise value of the slope depends on the assumed stellar mass-to-light ratio of the BCG.

As with the X-ray studies, gravitational lensing alone is unable to separate the baryonic (luminous) and non-baryonic (dark) components. Given the observational evidence that BCGs often lie at the bottom of the cluster potential in regular, non-interacting systems (e.g. S01, G03, Jones et al. 1979), the dynamics of the stellar component offers a valuable route to resolving this problem. In practice, the stellar kinematics of the BCG provides an additional measure of the total mass at small radii. In work by Dressler (1979), the velocity dispersion profile of the BCG in Abell 2029 was found to rise significantly at large radii and this was taken as evidence that the cluster DM halo was being probed. More recently, Kelson et al. (2002) have measured an extended velocity dispersion profile in the BCG in Abell 2199, for which they concluded that the best-fitting DM density profile for the cluster was shallower than NFW. Miralda-Escudé (1995) first suggested that a combination of lensing and stellar velocity dispersion measurements could separate the luminous and dark components in the inner regions of clusters (see also Natarajan & Kneib 1996 for a lensing + dynamics analysis of Abell 2218). This article highlighted the system MS2137-23 which, at the time, was unique in containing both radial and tangential gravitational arcs.

In an earlier paper (Sand, Treu & Ellis 2002; hereafter STE02) we combined a simple axisymmetric lensing model of MS2137-23 with stellar velocity dispersion measurements of the BCG to place strong constraints on the inner slope of the DM density profile. The resulting β value was markedly inconsistent with $\beta \geq 1$ and we demonstrated carefully how the combination of lensing and dynamics offers superior constraints to those provided by either method alone.

The goal of this paper is to extend the results of STE02 to a larger sample of six galaxy clusters. In addition to MS2137-23 we consider two additional systems containing both radial and tangential gravitational arcs. The three other clusters contain only a tangential arc and analysis of this subsample offers a valuable control from which we expect to deduce whether selecting the rarer systems with radial arcs might bias our conclusions towards flatter inner slopes. As a further test on the robustness of our results, we check our lensing model by dropping the assumption of radial symmetry.

A plan of the paper follows. In §2 we discuss how the sample of clusters was chosen. In §3 we discuss the archival Hubble Space Telescope and further infrared imaging observations and how we derived the location of the critical lines and the surface photometry of the BCGs.

In §4 we present spectroscopic measurements made with the Keck telescope which delivered the redshifts of the gravitational arcs and the stellar velocity dispersion profile of the BCGs. We discuss our analysis of the DM density profiles in the context of the assumed mass model for both the radial+tangential and tangential-only arc subsamples in §5. In §6 we present a thorough discussion of possible systematic uncertainties associated with our method. In §7 and §8 we discuss and summarize our results, respectively.

Throughout this paper, we adopt r as the radial coordinate in 3-D space and R as the radial coordinate in 2-D projected space. We assume $H_0=65 \text{ km s}^{-1}\text{Mpc}^{-1}$, $\Omega_m = 0.3$ and $\Omega_\Lambda=0.7$.

2. Sample Selection

The aim of this project is to combine constraints from the velocity dispersion profile of a BCG with those from gravitational lensing to measure the slope of the inner DM density profile in galaxy clusters, as described in STE02. Two important simplifying assumptions inherent to our method are that the BCG lies at the bottom of the cluster potential, and that the BCG is a purely pressure supported system, whose dynamics can be described by the Jeans’ equation. For this reason, a suitable galaxy cluster for this project must have a dominant, relatively isolated central galaxy (coincident with the cluster’s center of mass) with nearby strong lensing features and no indications of significant substructure or a significantly elongated potential. Radial gravitational arcs – albeit uncommon – are particularly valuable since they constrain directly the derivative of the total enclosed mass (e.g. STE02).

In order to find a sample of suitable targets, we undertook an exhaustive search of the Hubble Space Telescope (HST) Wide Field and Planetary Camera 2 (WFPC2) archive for radial gravitational arcs in galaxy clusters. In summary, all galaxy cluster pointings in the redshift range $0.1 < z < 1.0$ were retrieved from the HST archive, ~ 150 different clusters in all. This is the first search of its kind and has yielded ~ 15 candidate radial arc systems. Dozens of smaller lensed features have been uncovered as well, due to the high angular resolution of HST.

We performed spectroscopic follow-up at the Keck Telescope of many candidate lensing systems, with emphasis on systems with both radial and tangential arcs. Spectroscopic confirmation is particularly important for radial arc candidates. In fact, since they normally occur in the very inner regions of galaxy clusters, they can easily be confused with optical filaments associated with cluster cooling flows. Indeed, several radial features proved to be contaminant optical filaments at the cluster redshift. A description of the search, the

complete catalog and spectroscopic identifications will be described in a follow-up paper (Sand et al. 2004, in preparation).

In this paper we focus on a sample of six spectroscopically confirmed lensing clusters, for which we have also obtained a stellar velocity dispersion profile of the BCG (Table 1). The sample includes three galaxy clusters with radial and tangential arcs and three clusters with just tangential arcs, one of which does not have HST imaging (MACS 1206; Ebeling et al. 2004, in preparation).

3. Imaging Data and Analysis

This section describes the two measurements that are to be made from the imaging data to determine the cluster mass distribution: the surface brightness profile of the BCG and the positions of the lensing critical lines as inferred from the location of symmetry breaks in the giant arcs. In addition, two of the six BCGs in our sample (RXJ 1133 and Abell 383) have obvious dust lanes. K-band images of the cluster centers were used to correct for the dust lanes and obtain the unreddened surface brightness profile of the BCG as described in §3.2. Table 1 is an observation log of all the optical/NIR observations.

3.1. Optical Data

Archival HST imaging is available for five of the six clusters. A gunn I-band image in good seeing conditions ($0''.7$ FWHM) was obtained for the final cluster, MACS1206, using the Echelle Spectrograph and Imager (ESI; Sheinis et al. 2002) at the Keck-II Telescope. Figure 1 shows the inner regions of the six clusters and their accompanying gravitational arcs. Superimposed on the images are the spectroscopic slit positions that will be described in §4.

Since our sample results from an extensive HST archive search, no specific observing strategy is common to all clusters. The HST observing strategies fall into two categories: 1) multiple-orbit observations separated by integer pixel dithers (MS 2137-23, Abell 383, and Abell 963) and 2) single orbit SNAP observations comprising two CR-SPLIT, undithered exposures (Abell 1201, RXJ 1133). Accordingly, two different data reduction procedures were employed.

The clusters with dithered exposures were pipeline processed with the DITHER package (Fruchter & Hook 2002) in IRAF to remove cosmic rays, correct for the undersampling of the point spread function, and to shift and combine the frames. The effective resolution for

the images (F606W and F702W) was $\sim 0''.15$. The undithered targets were processed by first applying the IRAF task WARMPIX using the table data supplied by the WFPC2 website for the dates of the observations. The images were then combined with the task CRREJ to remove cosmic ray hits. A small number of residual cosmic rays were removed with the IRAF task LACOSMIC (van Dokkum 2001).

The single, Gunn I band exposure of MACS 1206 was reduced in a standard way with cosmic ray removal being performed by the IRAF task LACOSMIC (van Dokkum 2001). Photometric calibration, good to 0.03 mag, was obtained from two photometric standard star fields (Landolt 1992).

3.2. Near-infrared Data

Dust features in BCGs are common (see e.g. Laine et al. 2002), but hinder attempts at measuring structural parameters. To correct for internal dust extinction in Abell 383 and RXJ 1133, we observed the two BCGs with NIRC on the Keck I Telescope in the K_s band (see Table 1 for the observing log). The data were reduced in a standard manner using IRAF tasks to dark subtract, linearize, flat-field, align and combine the individual frames. The flat-fields were created from a rolling median of the adjacent science frames. The point-spread-function of both final reduced frames has FWHM $\simeq 0.6''$.

A dust correction is obtained as described in Treu et al. (2001) and Koopmans et al. (2003). Briefly, we first assume that dust has a negligible effect at large radii and that any intrinsic BCG color gradient is small. Then we smooth the HST image to the resolution of the K-band image, and compute an extinction map in the observer frame:

$$E_{HST,K}(x, y) = \mu_{HST}(x, y) - \mu_K(x, y) - \mu_{HST,K}(\infty), \quad (1)$$

where $\mu_{HST}(x, y)$ and $\mu_K(x, y)$ are the surface brightness in a given pixel and $\mu_{HST,K}(\infty)$ is the color at large BCG radii. Adopting the Galactic extinction law of Cardelli, Clayton, & Mathis (1989; $R_V = 3.1$) we find the following relations between the absorption coefficients in the individual bands and the color excess (Eqn 1.). For Abell 383 $A_{F702W} = 1.199E_{F702W,K}$ and $A_K = 0.199E_{F702W,K}$. For RXJ1133 $A_{F606W} = 1.164E_{F606W,K}$ and $A_K = 0.164E_{F606W,K}$.

The correction removes any visible trace of the dust lane. However, it reveals that the BCG in Abell 383 has a very close, compact companion. For the purpose of surface photometry analysis, the close companion is easily dealt with by fitting it simultaneously to the BCG. The companion is $\sim 0''.7$ from the center of the BCG and is ~ 5.5 mag fainter with $R_e \simeq 0''.5$. The spectrum of the companion and the BCG cannot be distinguished in the ESI

spectrum so no relative velocity can be measured. Assuming that the relative masses of the two galaxies is proportional to their flux ratio, the companion galaxy should not effect our later dynamical analysis.

3.3. Surface brightness fitting

Total magnitudes and effective radii (R_e) were measured from our (dust corrected) optical images by fitting two dimensional $r^{1/4}$ surface brightness profiles as described in STE02 using the software developed by Treu et al. (1999, 2001). For the purpose of the fitting, $r^{1/4}$ models were convolved with artificial Point Spread Functions (PSFs). Tiny Tim (Krist 1993) PSFs were used for the HST images, while gaussian PSFs were adopted for the ground based images. Note that uncertainties in the artificial PSF have negligible impact on the determination of the effective radii which are always much larger than the PSF HWHM (c.f. Treu et al. 2001). Figure 2 shows the measured surface brightness profile along with the best fitting $r^{1/4}$ fit (PSF convolved).

Observed magnitudes were corrected for galactic extinction using the $E(B - V)$ values and extinction coefficients calculated by Schlegel, Finkbeiner & Davis (1998). Finally, observed magnitudes were transformed to rest frame absolute magnitudes through the standard filter that best matches the observed bandpass through a K-color correction as in STE02 and Treu et al. (1999,2001). Typical error estimates on the transformation are of order 0.05 mag. All BCG photometric results (both rest and observed frame) are listed in Table 2.

3.4. Critical line determination

Crucial to the simple lensing method that we describe in § 5.1 is the location of the lensing critical line (either radial or tangential). Formally, the critical lines of a lens model are those regions where the magnification of the images diverge, although this does not occur in practice due to the extended size of the source. In addition to being strongly magnified, objects near the radial critical line will be distorted strongly in the direction radial to contours of constant density, while objects near the tangential critical line will be distorted tangentially. Typically, giant bright arcs are the result of multiple highly magnified merging images. Two merging images with opposite parity often bracket a critical line.

In this work, the critical line position was chosen by visual inspection, either in between two merging images or near strongly distorted arcs. No prior lensing analysis was done, although for those systems that have published lens models this extra information was taken

into account. The critical line positions including conservative estimates of the uncertainties are listed in Table 3. Note that the radial critical line uncertainties are larger due to contamination by the bright BCGs and the radial nature of these arcs. In contrast, the tangential critical line uncertainties are within a factor of ~ 2 -3 of the seeing disk.

4. Spectroscopic Data and Analysis

All spectroscopic measurements – yielding arc redshifts and/or a BCG velocity dispersion – were made with either the Low Resolution Imager and Spectrograph (LRIS) on Keck I (Oke et al. 1995) or ESI on Keck II (Sheinis et al. 2002). Table 4 summarizes the spectroscopic observations for each cluster.

4.1. Data Reduction

The LRIS data were reduced in a standard way with bias-subtraction, flat-fielding and cosmic ray rejection. Wavelength calibration was performed using calibration arc lamps and unblended sky lines. The instrumental resolution for the 600/5000 grism (blue arm, 560 dichroic) used for the velocity dispersion measurement of Abell 963 was measured to be 175 km s^{-1} from unblended night sky lines. For the ESI observations, a set of IRAF tasks (EASI2D) were developed for the specific goal of removing echelle distortions while preserving the two-dimensional shape of the spectrum. The instrumental resolution of the reduced 2D spectra for the $1''.25 \times 20''$ slit was measured to be 32 km s^{-1} from unblended night sky lines and the spatial scale ranges from 0.12 to 0.17 arcsec/pixel from the bluest to the reddest order.

EASI2D consists of the following steps: 1) Bad column interpolation, debiasing, and an initial flat-fielding are performed on the entire two dimensional spectrum. 2) The curved echelle orders are mapped using multi-hole exposures (spaced a constant 2.68 arcseconds apart (Goodrich, R & Radovan, M, private communication)) and multiple stellar exposures at prescribed positions along the slit. 3) Each order is rectified using the IRAF task TRANSFORM (conserving counts). Arc lamps and twilight sky flats are rectified along with science frames for further calibrations. 4) Sky flats are used to correct for the non-uniform sensitivity (slit function) in the spatial direction of the individual echelle orders. 5) After rectification, each exposure of each order is separated and cosmic ray cleaned using LACOSMIC. 6) After rectification, each order is separated and wavelength calibrated individually. 7) Sky subtraction is performed on each order interactively with a low order polynomial fit along the

spatial direction to blank regions of the slit. Alternatively, sky subtraction can be achieved by subtracting appropriately scaled dithered science exposures from each other. This second method is preferable beyond $\sim 7000\text{\AA}$ where sky emission lines are strongest. 8) If needed, one dimensional spectra can be extracted from the two-dimensional spectra of each order and combined on a single spectrum. This step was typically undertaken only for the kinematic template star spectra (see § 4.2).

4.2. Redshift measurements and stellar kinematics

Table 1 (BCGs), Table 3 (gravitational arcs) and Figure A.2 details all of the redshift measurements made. Many of these measurements were dependent on the high spectral resolution of ESI, since many emission lines were buried in the OH sky background. All arc redshift identifications are based on the detection of the [OII]3726,3729 doublet in emission. Note that, for the purpose of this work, we are only using the “northern” arc of Abell 963 (Ellis, Allington-Smith & Smail 1991). Abell 383 has also been studied extensively by S01 (see also Smith 2002 and Smith et al. 2004, in prep.), who obtained a spectroscopic redshift for the tangential arc in this cluster. We add to S01’s study by measuring spectroscopic redshifts for both the radial arc and a different portion of the tangential arc. These new data provide more stringent constraints on the gravitational potential of this cluster (§6.1).

We now describe the measurement of the line of sight velocity dispersion profile of the BCGs. The 2D spectra were summed into spatial bins corresponding approximately to the seeing during the observation, thus ensuring that each velocity dispersion measurement is approximately independent, and increasing the signal-to-noise ratio per spatial bin. In Abell 383, an entire side of the spectrum was avoided due to the interloping galaxy (§3.2) and the presence of the dust lane. Also, we avoided the side of the BCG in RXJ 1133 effected by the dust lane. For Abell 1201 two slightly different position angles were used.

Following well established procedures (Franx 1993; van Dokkum & Franx 1996; Treu et al. 1999,2001; Kelson et al. 2000; van Dokkum & Ellis 2003; Gebhardt et al. 2003), the velocity dispersion for each spatial bin is measured by comparing stellar templates (appropriately redshifted and smoothed to the instrumental resolution of the galactic spectra) broadened by Gaussian line profiles with the galactic spectrum. The fit is performed using the Gauss-Hermite Pixel Fitting Software (van der Marel 1994) in pixel space to allow for easy masking of emission lines and regions of high night sky residuals. All velocity dispersion measurements were taken from spectral regions around the G band absorption feature. Also measured with the Gauss-Hermite Pixel Fitting Software was the relative velocity profile of each BCG. There is no evidence of rotation (within the uncertainties) in any of the BCGs

and so we will assume in our analysis that the systems are completely pressure supported.

For each BCG, the velocity dispersion profile was measured using all of the available stellar templates with a variety of continuum fits. The stellar template that yielded the lowest χ^2 was adopted as the best fit. Table 5 contains the tabulated velocity dispersion measurements obtained. Listed uncertainties are the sum in quadrature of a random component (taken from the output of the Gauss-Hermite Pixel Fitting Software) and a systematic component due to template mismatch (the rms of the velocity dispersion obtained from all templates).

In order to measure accurate velocity dispersions, spectra with sufficient S/N are required. In general, the minimum S/N needed depends both on the instrumental resolution and the velocity dispersion to be measured. A higher S/N is needed as the velocity dispersion becomes comparable to and less than that of the instrumental resolution (e.g. Treu et al. 2001; Jorgensen, Franx & Kjaergaard 1995). Since the typical central velocity dispersion of a BCG is $\sigma \sim 300\text{-}400 \text{ km s}^{-1}$ (e.g. Fisher, Illingworth, & Franx 1995) compared to the 32 (175) km s^{-1} resolution of the 1''25 (1''50) ESI (LRIS) slit the velocity dispersion measurement should be reliable down to low S/N. In order to verify this numerically for the case of the ESI configuration, high S/N template spectra were broadened by Gaussian line profiles to known velocity dispersions ($\sigma = 50, 100, 150, 200, 250, 300, 350 \text{ km s}^{-1}$) and Poisson noise was added (S/N= 5, 7, 10, 12, 15, 20) for a hundred different realizations. The velocity dispersion of these broadened, noisy spectra was then recovered using an area around the G band absorption feature with the Gauss Hermite Pixel Fitting software with both the same template (K0III) and a template with a different spectral type (G9III template used on a broadened K0III spectrum). Using the K0III template on the broadened K0III spectrum recovers the expected velocity dispersion with formal uncertainties less than 10% down to S/N of 5 (the exception being the 50 km s^{-1} measurement with S/N=5, which had an average formal uncertainty of 8 km s^{-1}). Using the G9III template on the K0III broadened spectrum did lead to systematic offsets from the input velocity dispersion of up to 6.5%, comparable to the formal uncertainty in the measurement. Thus, we will take into account possible uncertainties with regard to template mismatch in the data both in our final uncertainties and when deriving mass profiles.

5. Analysis and Results

We now combine the observed photometric and spectroscopic properties of the BCG and giant arcs to constrain the luminous and DM distribution in the central region of the clusters. In particular, the goal of this analysis is to determine the range of inner DM density

slopes permissible and to compare these to predictions from numerical CDM simulations. The key to this method is to combine the constraints on the mass from the velocity dispersion profile with that from lensing to get a better overall measurement than can be made with each individual technique. The method used is identical to that employed by STE02, with improved numerical accuracy. There is no change in our basic conclusions on MS2137-23 from that work.

5.1. Mass Model and overview of the fitting procedure

We adopt a spherically symmetric two component mass model comprising the BCG and cluster DM halo. We assume that the BCG is coincident with the bottom of the cluster potential. To describe the luminous BCG component we used a Jaffe (1983)

$$\rho_L(r) = \frac{M_L r_J}{4\pi r^2 (r_J + r)^2}, \quad (2)$$

mass density profile with total mass M_L and $R_e = 0.76r_J$. A Jaffe profile reproduces well the actual surface brightness profiles of the BCGs in our sample and has the extra advantage of giving analytic solutions to the surface brightness profile and line of sight velocity dispersion. We assume that a single mass-to-light ratio describes well the stellar component of the mass. For a given stellar M_*/L both M_L and r_j can be deduced from the observed surface photometry. We also investigated the effects on the inner DM slope by changing the luminous mass density profile to a Hernquist profile (Hernquist 1990) in §6.3 as a robustness check of our results. Note that the PSF convolved Hernquist and Jaffe luminous matter distributions bracket the observed data in all of our clusters (see § 6.3 for a discussion).

The cluster DM halo is modeled as

$$\rho_d(r) = \frac{\rho_c \delta_c}{(r/r_{sc})^\beta [1 + (r/r_{sc})]^{3-\beta}}, \quad (3)$$

which is a generalization of the numerically simulated CDM halos, with ρ_c being the critical density and δ_c a scaling factor. This density profile asymptotes to $r^{-\beta}$ at $r \ll r_{sc}$ and r^{-3} at $r \gg r_{sc}$. For values of $\beta = 1, 1.5$, the DM density profile is identical to that found by NFW and nearly identical to that of M98, respectively; and thus using this general form for the DM halo allows for direct comparison to numerical results.

Considering the observations made, there are four free parameters in our mass model: (1) the stellar mass-to-light ratio, M_*/L , (2) the inner slope of the DM profile β , (3) the DM density scale δ_c , and (4) the DM scale radius r_{sc} . In general, r_{sc} is much larger (greater than 100 kpc) than our most distant mass probe, tangential gravitational arcs (Bullock et al.

2001; Tasitsiomi et al. 2003; see also Wu & Xue 2000). Given this, the location of the critical lines then only depend slightly on r_{sc} , since it is the projected mass that is important. In our modeling we set $r_{sc}=400$ kpc leaving only three free parameters. The value of r_{sc} was chosen as a typical value seen in galaxy cluster numerical simulations for a typical cluster with virial radius of ~ 2 Mpc (see discussion in § 6.3). Much larger values of r_{sc} seem to be ruled out on observational grounds as well (Gavazzi et al. 2003; Kneib et al. 2003; Wu & Xue 2000). In §6.3 we show that allowing r_{sc} to vary within reasonable bounds as proscribed by CDM simulations has a small effect on our β measurement, but that the effect is comparable to our other systematics.

We discuss in detail the analysis of both the lensing and velocity dispersion data in the Appendix. We briefly describe the method here. By comparing the observed position (and its uncertainty) of gravitational arcs with the predicted position of the arcs (given a set of free parameters, $\{M_*/L, \beta, \delta_c\}$) a likelihood function can be calculated over the appropriate parameter space. Similarly, the observed velocity dispersion profile (which depends on the mass enclosed at a given radius and the relative contribution from luminous and dark matter) for a BCG in a cluster can be compared with that expected for a given set of free parameters (taking into account the seeing and spatial binning of the observations) and another likelihood function can be calculated. The total likelihood for a given set of free parameters is simply the product of the lensing likelihood and the stellar kinematics likelihood. In the next two subsections we discuss how we use these likelihood functions to place confidence limits on the inner DM density slope, β .

5.2. Radial Arc Results

The three clusters in our sample with radial and tangential arcs (hereafter known as the radial arc sample) allow for strong constraints to be placed on the DM density profile. The tangential arc provides a measurement of the projected mass enclosed at a given radius and the radial arc gives a measurement of the derivative of the projected mass enclosed at its radius.

Assuming that all underlying distributions are normal, we can use a χ^2 minimization technique to obtain confidence contours on our parameter estimates. This involves simply taking the χ^2 difference at any point in parameter space with respect to the minimum χ^2 . Confidence contours in the M_*/L - β plane allow one to visualize acceptable β values as a function of the mass of the BCG. After marginalization with respect to δ_c , the 68, 95, and 99% confidence contours in the M_*/L - β plane were placed at a $\Delta\chi^2=2.30, 6.17, \text{ and } 9.21$ respectively. Figure 3 (top row) shows the contours obtained for our radial arc sample.

To constrain the inner slope β alone, we further marginalized with respect to M_*/L . The resulting probability distribution function (PDF) for β for all three clusters is shown in Figure 5. We adopt the peak of the distribution as best estimate of the parameters. Confidence intervals are obtained by integrating the PDF above a threshold such that the total area under the curve is 68% (95%) of the total. Doing this, we found $\beta=0.57_{-0.08}^{+0.11}$ ($_{-0.17}^{+0.25}$) for MS2137-23, $0.38_{-0.05}^{+0.06}$ ($_{-0.11}^{+0.12}$) for Abell 383, and $0.99_{-0.14}^{+0.18}$ ($_{-0.28}^{+0.28}$) for RXJ 1133.

Note immediately that the intervals for the individual clusters do not overlap at the 68% level. Therefore we conclude that there is significant intrinsic scatter in the inner slopes of the DM halos. To assess the scatter in β values that we find in the radial arc sample, we calculate the standard deviation without account of the corresponding PDF and find $\Delta\beta \sim 0.3$. The scatter and its possible consequences will be discussed in § 7.2.

Having noted the existence of significant intrinsic scatter, we can determine the average inner slope of DM by looking at the joint radial PDF, obtained as the product of the three individual distributions (shown in Figure 5 as a solid line; note that this measure is analogous to the weighted average). We find that the average inner slope and related uncertainty are $\beta = 0.52_{-0.05}^{+0.05}$ ($_{-0.10}^{+0.11}$). Assuming that our sample of clusters is representative of the entire cluster population this means the average slope is inconsistent at $> 99\%$ CL with both the NFW and Moore profile.

5.3. Tangential Arc Results

Before discussing the radial arc results any further we consider the issue of sample selection bias in more detail. Are radial arc clusters a representative subsample of relaxed clusters as far as DM inner slopes are concerned? It is well known that total density distributions that are steeper than $\rho \propto r^{-2}$ do not produce radial arcs (e.g. Hattori, Kneib & Makino 1999). Thus, if there is a wide range in the distribution of inner slopes, by selecting radial arc systems we might be rejecting the more cuspy systems. This bias (hereafter the radial arc selection bias) might be exacerbated by the fact that the radial arcs in our sample are buried in the BCG, a steep density profile in its own right. We investigate how robust our results on β are with respect to our choice of luminous density profile in § 6.3.

A clean and powerful way to address this issue is to obtain a control sample of tangential arc-only systems (hereafter the tangential arc sample). This will enable us to determine if the radial arc systems appear to be outliers in the general cluster population. At the same time this tangential arc sample will provide an additional – albeit less precise – measurement of the DM inner slope.

The bottom row in Figure 3 and 6 display the results for the tangential arc sample. This was subject to the same analysis as for the radial arc sample with the exception that we adopted a prior to ensure that the DM profile is monotonically declining with radius ($\beta \geq 0$). Note in fact that the results always go toward $\beta=0$ for the tangential arc sample, at variance with the results for the radial arc sample. In fact, the shapes of the confidence contours in the M_*/L - β plane are markedly different from the analogous contours for the radial arc sample (see § 5.4). We calculated upper limit confidence levels on β , since the shape of the probability distribution function lends itself to this type of interpretation. The 68% (95 and 99%) upper limits are $\beta = 0.29$ (0.62, 0.82), 0.40 (0.67, 0.77), and 0.43 (0.80, 0.97) for Abell 1201, MACS 1206, and Abell 963 respectively. The joint tangential arc distribution has 68, 95, and 99% confidence upper limits of $\beta=0.20$, 0.43, and 0.57 respectively.

Is the radial arc sample probing an outlier population of galaxy clusters due to the fact that radial arcs cannot form in systems with density distributions steeper than $\rho \propto r^{-2}$? In the following we assume that the joint distribution for each sample is a fair representation of the underlying distribution, despite the sample size. As can be seen from Figure 6, the radial arc sample does not have a shallower DM density profile than the tangential arc sample, as would be expected if there was a radial arc bias. To compare the two samples we convolved the radial and tangential arc sample probability distribution functions in order to compute the probability distribution function for the variable $\beta_r - \beta_t$, where the subscripts represent the radial and tangential arc sample values of β . Due to the one-sided nature of the tangential arc probability distribution function, it is appropriate to use upper limits to quantify the confidence region of the variable $\beta_r - \beta_t$. The value of $\beta_r - \beta_t$ is less than 0.45 and 0.57 with 68 and 95% confidence, respectively. The probability that $\beta_r - \beta_t$ is less than 0 (as would be expected if there was a radial arc bias) is $\sim 2\%$. There is no indication of radial arc bias, and the radial and tangential arc samples are reasonably consistent given the small number of systems.

5.4. Summary of results

We have presented new measurements of the inner slope (β) of DM halos in clusters of galaxies, considering a sample of three radial arc systems and a sample of three tangential arc systems in carefully chosen relatively relaxed clusters.

The main results from the radial arc systems are: (i) the average $\langle \beta \rangle = 0.52 \pm 0.05$ is much smaller than that suggested by numerical DM only simulations (either NFW or Moore); (ii) our precision allows us to determine a first measurement of the intrinsic scatter in β , which we estimate to be $\Delta\beta \sim 0.3$; and (iii) individual clusters can be as cuspy as

NFW (RXJ1133). The results from the tangential arc sample confirm and reinforce our findings: (i) the upper limit to the average slope is $\beta=0.57$ (99% CL), again much smaller than numerical simulations (NFW or Moore); (ii) although with larger uncertainties, the results from the tangential arc sample are statistically consistent with those from the radial arc sample, confirming that our results are not affected by a radial arc selection bias.

Before moving on to discuss in detail the comparison with numerical simulations and consider the broader implications of these results (§7), we need to address two further issues. First, we would like to discuss in greater detail our method, understanding at least qualitatively some of its features. This will hopefully provide an element of physical intuition in addition to the statistical analysis. Secondly, we need to make sure that systematic uncertainties are not dominating our error budget, which so far includes only random uncertainties. The first point is the subject of the remainder of this section. Section 6 is devoted to a careful analysis of all known systematics and related uncertainties on β .

The joint fitting of the lensing and velocity dispersion data greatly enhances our ability to distinguish between DM profiles (see STE02). The top left panel of Figure 7 illustrates why that is the case. The hatched boxes represent the velocity dispersion measurement for MS2137-23 and their $1\text{-}\sigma$ uncertainties. The solid black curve shows the best fitting velocity dispersion profile model obtained with our combined lensing and velocity dispersion analysis. The dashed curve shows a velocity dispersion profile for a set of free parameters that agrees extremely well ($\Delta\chi^2 < 1$; $\beta=1.30$) with the gravitational lensing measurements alone, but does not match the measured velocity dispersion profile of the BCG. This special case (where the $M_*/L=0$ indicates that the luminous component is a massless tracer of the potential) clearly shows how mass models with too steep an inner profile cannot both match the velocity dispersion profile measurement and reproduce the positions of the gravitational arcs. The remaining panels in Figure 6 plot both the observed and best-fitting velocity dispersion profile for each of the six clusters.

Our best-fitting mass models produce density profiles that are remarkably similar in their makeup (see Figure 7). On $\lesssim 10$ kpc scales, the matter distribution is dominated by the luminous, BCG component, with the DM component dominating at larger radii. Dubinski (1998) has found a similar result by numerically simulating the formation of a BCG in the presence of a cuspy DM halo. As can be seen from Figure 7, the velocity dispersion measurement of the BCG allows us to probe the matter distribution where luminous matter is important, while the gravitational arcs probe regions where DM dominates. The measurement techniques complement each other.

It is appropriate to assess the goodness-of-fit of our best-fitting models. While $\Delta\chi^2$ is distributed as a χ^2 distribution with three degrees of freedom (representing the three

free parameters in our model), the best-fitting model (with χ_{min}^2) is distributed as a χ^2 distribution with $N - 3$ degrees of freedom, where N is the number of data points and three again represents the number of free parameters (see e.g. Press et al. 1997). The total best-fitting χ^2 for each cluster is: Abell 383, $\chi^2/dof=8.3/2$; MS2137-23, $\chi^2/dof=8.9/7$; RXJ 1133, $\chi^2/dof=1.0/2$; Abell 1201, $\chi^2/dof=6.6/6$; Abell 963, $\chi^2/dof=2.9/3$; MACS 1206, $\chi^2/dof=1.4/1$. Of the total, the contribution from the gravitational lensing portion of the χ^2 is never more than 0.2, meaning that the bulk is due to the velocity dispersion profile (see Figure 6 for the best-fitting velocity dispersion profiles). The one cluster with a relatively high χ^2 is Abell 383. However, given the simplicity of our mass model, this relatively high χ^2 should not be alarming. In section 6 we explore in detail possible systematic effects in our current analysis, any of which could be responsible for a less than perfect fit to the data. Since all of these systematic checks indicate that $\Delta\beta \lesssim 0.2$, we are confident in the robustness of our results.

What causes the difference in the confidence contour shapes in the M_*/L - β plane between the radial arc sample and the tangential arc sample? Both samples do not allow a steep DM inner density profiles because of their inability to match the observed BCG velocity dispersion profiles described in the previous paragraph. However, it seems as if the radial arc sample is capable of pinpointing the DM inner density slope, while the tangential arc sample can give just an upper limit. Due to the functional form of the radial eigenvalue (see Eqn. A5), radial arcs cannot form in total density profiles steeper than $\rho \propto r^{-2}$. For our mass model, as M_*/L increases and β becomes small, the above criteria for radial arc formation is not met unless the radial arc position is pushed out radially (where DM will have a larger contribution and thus soften out the effects of the cuspy luminous distribution) to a point where it is incompatible with its observed position. It is for this reason that low values of β are not allowed in the radial arc analysis and the DM inner density slope can be pinpointed.

The summary of the results presented in this subsection are at odds with predictions of CDM simulations and have claimed to measure the intrinsic scatter in the inner DM slope, β . In order for such results to be taken seriously, it is imperative that our method is tested thoroughly with respect to our simplifying assumptions. It is our goal in the next section to test systematically all of our assumptions before we discuss the implications of our results for CDM.

6. Systematics

During the course of our analysis, many simplifying assumptions were made. As an exploratory study aiming to obtain tight constraints on the DM density profile, we strived to simplify our model and its inputs while still extracting the correct inner density profile. However, it is possible that these simplifications are giving systematically different values of the DM inner density slope than a more complex modeling. To judge the robustness of our method we have performed a battery of tests. First, in § 6.1, we explore the fact that we neglected both ellipticity and substructure in our lensing treatment. Second, in § 6.2, we look at possible complications in our analysis of the BCG dynamics (e.g. orbital anisotropy and template mismatch). Finally, in § 6.3 we report on tests run to check our results depending on changes in our luminous mass model and due to possible uncertainties in our measurements. Abell 383 has the tightest constraints in our sample (see § 5.2) and by using it to illustrate our test results (in § 6.2 and § 6.3) we demonstrate the impact our assumptions have on our determination of β .

6.1. Impact of Cluster Substructure and Ellipticity

Our cluster sample has been selected to comprise relaxed systems with no obvious signatures of strong ellipticity and/or bi-modality in their underlying mass distributions. Nevertheless, previous analyses of two of the clusters (Abell 383 and MS 2137-23) does reveal that they are not perfectly circular in projection (e.g. S01; Miralda-Escudé 2002). Our simple lensing method deliberately does not attempt to fit the detailed positions of all the multiply-imaged features of the clusters, concentrating instead on the positions of relevant critical lines, estimated from visual inspection of symmetry breaks in the observed multiple-images. In this section we exploit sophisticated two-dimensional lens models to investigate whether the simplifying assumptions in our one-dimensional models introduce any systematic bias into our results. Qualitatively, the key differences between the models discussed in this section and those upon which our main analysis is based is that in this section we include the ellipticity and substructure (arising from bright cluster ellipticals) of the clusters in the models, and also fit the models to all of the observed multiple-image systems.

We use the LENSTOOL ray-tracing software to construct a detailed model of each of the clusters in the radial arc sample. The details of this method are explained elsewhere, and we refer the interested reader to the relevant articles (Kneib 1993; Kneib et al. 1996; Smith 2002; Smith et al. 2004, in prep.). Briefly, we use the observed positions, redshifts, shapes and orientations of the observed multiple-image systems to constrain a model of the *total*

surface mass density in each cluster core. We stress that we do not attempt to decompose the best-fit total matter distributions into their respective dark and luminous components. Each model therefore consists of the minimum number of analytic matter components (each one parametrized as a truncated pseudo-isothermal elliptical mass-distribution – Kassiola & Kovner 1993; Kneib et al. 1996) required to fit the observables. In practice, each model contains a central dominant cluster-scale mass component that is centered on each BCG, plus an additional central mass component for the BCG, and a small number (≤ 4) of smaller mass components to account for contributions from likely cluster members that lie adjacent to the observed multiple-image systems. We briefly describe each model:

MS 2137-23 – This cluster has been extensively modeled by several authors (Mellier et al. 1993; Hammer et al. 1997; G03). We adopt STE02’s spectroscopic redshifts for the dominant tangential and radial arcs as constraints on our LENSTOOL model. A four component model is able to produce an acceptable fit to these constraints ($\chi^2/\text{dof} \simeq 1$). These components comprise the cluster-scale potential, the BCG and two galaxies lying $3''$ North-West of the BCG, adjacent to the radial arc (Fig. 1). This model predicts a central fifth image of the galaxy that appears as the giant tangential arc that is in broad agreement with that predicted by G03’s model. However when subtracting a model of the BCG from the *HST* frame, we are unable to confirm G03’s claimed detection of the fifth image. We therefore do not include this image as a constraint on the model. The ellipticity of the best-fit fiducial model is $\epsilon = (a^2 - b^2)/(a^2 + b^2) = 0.18$.

Abell 383 – S01 constructed a detailed lens model of this cluster, based on their spectroscopic redshift of the brightest component (B0a) of the tangential arc (see also Smith 2002). We build on this analysis to add the spectroscopic redshifts of B1a/b and the radial arc into S01’s model. These new spectroscopic redshifts constrain the volume of parameter space occupied by the family of acceptable models. The best-fit model lies within the family of models identified by S01 as providing an acceptable fit to the data. Figure 8 illustrates the resulting lensing model for this cluster, showing the derived tangential critical curves for $z = 1, 3$. The detailed multiple-image interpretation of this cluster is described by Smith et al. (2004, in prep).

RXJ 1133 – We identify the tangential and radial arcs as comprising two images each of the background source. The compact high surface-brightness feature in the radial arc has a profile shape and FWHM similar to a point source. The origin of this point source is unclear since it does not appear in the other lensed images. It is likely a foreground star, or possibly a transient event in the lensed galaxy that only manifests itself in the radial arc due to time delays. To obtain an acceptable fit to the lensing constraints, we use a five component model: cluster-scale potential, BCG, two dwarf galaxies adjacent to the fifth image and the

moderately bright likely cluster member $7''$ away from the BCG directly opposite these two dwarfs. The ellipticity of the best-fit fiducial model is $\epsilon = 0.19$.

After obtaining the best-fit fiducial lens model for each cluster, we systematically explored the parameter space of each model to determine the family of acceptable models ($\Delta\chi^2 \leq 1.0$). We then compare this family of models with the family of acceptable models with $\Delta\chi^2 \leq 1.0$ (projected from 3D to 2D) from the analysis presented in §5.2 (this is equivalent to the 68% confidence interval for one parameter). Fundamentally, the lensing constraints contain information about the enclosed mass at the position of the tangential arcs and the derivative of the projected mass enclosed at the position (i.e. symmetry break between the two components) of the radial arc. We extract azimuthally averaged projected density profiles from these two sets of models for each cluster and compare $M(\leq R_{\text{tangential}})$ and $d(M/R)/dR(R_{\text{radial}})$, taking due account of the uncertainties in the determinations of $R_{\text{tangential}}$ and R_{radial} .

We plot the results of this comparison in Fig. 9. The difference in $M(\leq R_{\text{tangential}})$ between the two methods is never more than 8% of that of the LENSTOOL result. Note that the 1D method presented in this work is robust in its measurement of β when the position of the tangential critical line is shifted $\pm 0.5''$ (see §6.3). A shift in the tangential critical line position is equivalent to changing $M(\leq R_{\text{tangential}})$, and so we defer to that subsection for a discussion of how a mismeasurement of $M(\leq R_{\text{tangential}})$ effects our conclusions on the DM density profile.

We concentrate here on the radial arc comparison, focusing on the discrepancy identified in MS2137-23 (the most discrepant in the sample). In the following we will assume that any correction necessary in the method is solely a correction that must be made to the DM component. This is certainly a very conservative estimate since the luminous BCG mass component contributes significantly on the scales of the radial gravitational arcs. For simplicity, we assume that we are dealing with power-law surface density profiles, $\Sigma(R) \propto R^\gamma$. This implies that $M(< R) \propto R^{\gamma+2}$ and $\rho(r) \propto r^{\gamma-1}$. In MS2137-23 $\gamma = -0.29$ and -0.50 for the method in this work and the LENSTOOL results respectively, at the position of the radial critical line. A systematic mismeasurement of $\Delta\gamma = 0.2$ will cause a similar sized mismeasurement in the value of β , $\Delta\beta = 0.2$. This is roughly twice the size of the random error component ($\beta = 0.57^{+0.11}_{-0.08}$) quoted in §5.2 for MS2137-23. Note that the correction implied from the LENSTOOL analysis is in the direction of lower β values, even further away from predictions made by CDM numerical simulations. We conclude that any systematic effect due to the axisymmetric lens modeling in this work can affect our β measurement by of order the random error components we have calculated.

To aid comparison of our empirical measurements with future observational and theoret-

ical studies, we list here the values of γ , assuming that $\Sigma(R) \propto R^\gamma$. Using the 1-D approach presented in this work, $\gamma(R_{radial}) = -0.29 \pm 0.03$ for MS2137-23, -0.43 ± 0.05 for RXJ1133 and -0.36 ± 0.03 for Abell 383. With the 2D LENSTOOL analysis $\gamma(R_{radial}) = -0.50 \pm 0.01$ for MS2137-23, -0.33 ± 0.10 for RXJ1133, and -0.43 ± 0.02 for Abell 383.

6.2. Velocity Dispersion Measurements & Modeling

In §4.3 we presented the velocity dispersion measurements such that the final uncertainty tabulated in Table 5 is the addition in quadrature of a random component (taken from the output of the Gauss-Hermite Pixel Fitting Software) and a systematic component associated with template mismatch. Template mismatch is due to the fact that we used a single stellar spectral type to determine the kinematics of the BCGs. We quantified the effect of template mismatch in §4.3 by taking the rms deviation among the different stellar templates used to represent a possible systematic offset. While we incorporated this uncertainty into our mass modeling analysis, it is nonetheless necessary to understand how robust our results are to systematic offsets of the velocity dispersion profile. For each BCG we shifted the measured velocity dispersion profile up and down by the systematic uncertainty (typically $\sim 15\text{-}20 \text{ km s}^{-1}$) and reran our analysis to determine the impact on our results. The typical shift in the $M_*/L\text{-}\beta$ plane is about $\Delta\beta \sim \pm 0.15$, and we conclude that template mismatch can not greatly alter our final results.

In our dynamical modeling of the BCGs we assumed isotropic orbits (see Appendix A.2) for the constituent stellar tracers. This assumption is justified on several grounds. From an observational point of view, Kronawitter et al. (2000) found that in their sample of galaxies the best-fitting models were nearly isotropic with typical $\alpha \simeq 0.3$ (α is the anisotropy parameter, see Appendix Eqn. A8) at $R_e/2$, falling to $\alpha = 0$ at larger radii. There was little indication of any tangential ($\alpha < 0$) anisotropy in that study. Gerhard et al. (2001) obtain complementary results from an extended sample. Similar conclusions have been obtained theoretically (e.g. van Albada 1982), with strong radial anisotropy leading to instability (Merritt & Aguilar 1985; Stiavelli & Sparke 1991).

Nonetheless, it is still instructive to rerun the analysis with anisotropy, especially radial anisotropy. Using an anisotropy radius, r_a (implementing the Osipkov-Merritt parametrization, Eqn. A8), equal to $0.5r_j$, approximately at the point where observations have indicated that orbits are somewhat radially anisotropic, we have investigated the effects on our confidence contours. Note that with this parametrization, stellar orbits become more and more radially anisotropic with increasing radius. The confidence contours in the $M_*/L\text{-}\beta$ plane move towards lower acceptable values of β ($\Delta\beta \sim -0.20$ for $r_a = 0.5r_j$; see Fig. 11), in-

creasing the disagreement with predictions of N-body simulations. We conclude that modest radial anisotropy will only strengthen our claim that the observed DM profiles are shallower than predicted theoretically.

Likewise, we have introduced a constant tangential anisotropy of $\alpha = -0.5$. Observationally, tangential anisotropy in the inner regions of giant ellipticals is very rare (e.g. Kronawitter et al. 2000; Gerhard et al. 2001). As expected, the results indicate a slight steepening of the DM halos ($\Delta\beta \sim +0.20$; see Fig. 11). Given the extreme case presented here, we conclude that our results are robust to slight tangential anisotropy in the BCG.

In this work we have used Gaussian line profiles to represent the line-of-sight velocity dispersions of the BCGs. This approach provides a good low-order fit to galactic spectra, but in the outer parts of galaxies deviations from Gaussian can be of order $\sim 10\%$ leading to systematic mismeasurements of rotation velocities and velocity dispersions of the same order (van der Marel & Franx 1993). Higher order velocity moments are routinely measured for nearby galaxies giving information on their orbital structure (e.g. Kronawitter et al. 2000; Gerhard et al. 2001; Carter, Bridges, & Hau 1999). In the inner regions of galaxies, these studies have indicated that deviations from a Gaussian line profile are small, especially on the scales probed in this work ($\lesssim 0.5R_e$). However, to make these measurements, high signal-to-noise is needed, and this makes it hard to measure these parameters at even modest redshift due to cosmological surface brightness dimming. For this reason, we were unable to measure deviations from Gaussian line profiles in even the central regions of the BCGs. Any systematic introduced due to the Gaussian line profiles used must be small on the scales we are probing. Earlier in this section we have shown that our results are robust to orbital anisotropies (which would lead to deviations from Gaussian line profiles). Miralda-Escudé (1995) suggested that in the rapidly rising portion of the velocity dispersion profile expected from BCGs at large radii (see e.g. Fig. 6) that deviations from Gaussian line profiles should be expected, even in systems with isotropic orbits. At the moment, this can only be verified in nearby BCGs where higher-order moments could be measured to high radii, beyond the scales probed in this work.

6.3. Other Assumptions and Measurement Uncertainties

We have subjected our data to several additional tests. We changed the luminous mass model to a Hernquist profile, systematically altered the seeing by 30%, adjusted R_e of the BCG by 10%, modified the scale radius of the DM halo, r_{sc} , and shifted the radial and tangential critical lines. All tests were performed by changing one parameter at a time. We report the results of these tests below.

(1) We replaced the Jaffe luminous density profile with a Hernquist profile to see how robust our constraints on β are with respect to our choice of the Jaffe density profile for the BCG. We have chosen the Jaffe and Hernquist profiles because they give analytic solutions to the surface brightness profile and line of sight velocity dispersion. As can be seen from Figure 2, the Jaffe and Hernquist profile bracket the data at low radii ($< 1''$). The Hernquist luminous mass density profile goes like $\rho \propto r^{-1}$ at small radii. A Jaffe density profile is slightly more cuspy than an $r^{1/4}$ profile, while a Hernquist profile is slightly less cuspy. We obtained confidence contours in rough agreement with the original mass model. However, a Hernquist profile give a much larger best-fitting χ^2 ($\Delta\chi^2 \sim 10$ with respect to the best-fitting Jaffe luminous density profile results). Since we are bracketing the true surface brightness profile with our Jaffe and Hernquist parameterizations and we get roughly equivalent results on β , we are confident that our choice of the Jaffe luminous distribution is not biasing our results towards shallow DM halo profiles.

(2) We argued in § 5.1 that our final results are not very sensitive to the scale radius, r_{sc} , that we assume for the DM density profile, although there should be some dependence due to projection effects. Since it is the goal of this work to test the predictions of CDM, it is important that a range of r_{sc} compatible with numerical simulations are checked to make sure that this possible systematic is not large. Using the parameterization of the concentration parameter, c_{vir} , adopted by Bullock et al. (2001) for a $\sim 10^{15} M_{\odot}$ halo with $R_{vir} \sim 2$ Mpc, we expect r_{sc} to lie between 240 and 550 kpc (68% CL). Recently, Tasitsiomi et al. (2003) have simulated fourteen cluster-sized DM halos having cuspy profiles with mean r_{sc} of 450 ± 300 kpc. These values seem reasonable observationally, as well. For example, G03’s best fitting NFW profile for MS2137-23 using weak lensing had $r_{sc} = 67^{+300}_{-24}$ kpc. As a test, we briefly considered r_{sc} as a fourth free parameter, taking a flat prior on r_{sc} between 100-800 kpc, in accordance with the range of r_{sc} found by Tasitsiomi et al. (2003). After marginalization with respect to the other free parameters, this analysis caused a shift of $\Delta\beta \sim 0.15$ towards steeper values of β , giving us confidence that for reasonable values of r_{sc} our constraints on β are robust.

(3) Since the seeing is one of the measured inputs in the velocity dispersion portion of the analysis (see Eqn. A11 in the Appendix), we changed the seeing value by $\pm 30\%$ to determine how robust our conclusions are to mismeasurements in the seeing. We found shifts of $\Delta\beta \sim 0.05$ and thus concluded that even significant mismeasurements in the seeing do not effect our final results.

(4) Additionally, we perturbed the positions of the effective radius of the BCG surface photometry fits by $\pm 10\%$. As mentioned earlier, mismeasurements in the luminous mass distribution could possibly alter the shape of the inferred DM halo. However, changing R_e

had a negligible effect on the measured confidence contours.

(5) Finally, although the visual measurement of the critical lines agrees to within $1\text{-}\sigma$ with those obtained from the 2D averaged results of the LENSTOOL analysis, we still tested to see how sound our results are to perturbations in the critical line positions. In our tests, both radial and tangential critical lines were perturbed by $\pm 0''.5$ from their reported positions. We found that changing the tangential critical lines by this amount had a negligible effect, while adjusting the position of the radial critical lines produced shifts on order $\beta \lesssim 0.1$. We conclude that our results are not extremely dependent on the exact location of the critical lines.

6.4. Summary of Systematics

In this section, we have performed a wide variety of tests to our model and mass measurement technique, with no test indicating that our method is incomplete or lacking. The main conclusions of these tests of the systematics can be summarized as follows:

(1) In § 6.1, we explored the consequences of our axisymmetric gravitational lens models by comparing our results with the sophisticated 2D ray-tracing software, LENSTOOL. A comparison suggests that at most our constraints on the inner DM density logarithmic slope are shifted by $\Delta\beta \sim 0.2$.

(2) In § 6.2 we checked the robustness of our method in the face of possible systematics associated with the dynamics of the BCGs. Stellar template mismatch and orbital anisotropies can at most shift β by ~ 0.2 .

(3) In § 6.3 we performed a battery of tests to check our luminous mass model and our sensitivity to the observations. The most serious effect is associated with our assumed value of r_{sc} . For reasonable values of this parameter, the inner DM density logarithmic slope is shifted by $\Delta\beta \sim 0.15$.

Figure 11 plots the results for those tests performed in § 6.2 and § 6.3 that produce the largest changes in our estimation of β .

7. Discussion

7.1. Comparison with Simulations

The results of N-body simulations indicate that we should expect DM inner density profiles of between $\beta = 1$ and 1.5 even with the current refinements in modern N-body work that pay special attention to issues of convergence (e.g. Power et al. 2003; Fukushige et al. 2003). We have found a range of acceptable values of the inner logarithmic slope, with $\langle\beta\rangle = 0.52_{-0.05}^{+0.05}$, for our radial arc sample and $\beta < 0.57$ (at $>99\%$ confidence) for all three clusters in our tangential arc sample. We detect scatter in our radial arc sample, which we will discuss in § 7.2.

So what can account for the apparent discrepancy between observations and simulations? There are two questions that must be addressed. Do the scales probed in the observations correspond to those resolved in the simulations? Second, what effect do baryons have in our comparison?

In this work, we are only able to probe the mass distribution out to the distance of the tangential gravitational arc, which for our sample is <100 kpc. The original work by NFW97 had a gravitational softening radius of ~ 20 kpc (for their largest mass, galaxy cluster sized halos), although it is not clear that they achieved proper convergence down to this radius. Subsequent higher resolution work (e.g. Ghigna et al. 2000; Klypin et al. 2001) focused on the issue of convergence and reported that their results for the DM density profile were reliable down to scales of ~ 50 kpc at the cluster scale, both groups found $\beta \sim 1.5$. Even more recently, Power et al. (2003) and Fukushige et al. (2003) have performed extremely high resolution simulations, with density profile results reliable down to ~ 5 kpc ($\sim 0.002 R_{vir}$). Note that all of these works used different criteria for convergence. It seems safe to say that modern N-body simulations are becoming reliable down to the ~ 10 kpc scale for galaxy clusters, which is comparable to the scales being probed in this study. It is also comparable to R_e in a typical giant BCG, and so it is clear that baryons should play a more central role in further investigations.

It must be emphasized that these simulations include only collisionless CDM particles. It is unclear how baryonic matter, especially in regions where it may dominate the total matter density may affect the DM distribution. Several possible scenarios have been presented in the literature and the following discussion is not exhaustive. One possible situation, known as adiabatic contraction, is that as baryons sink dissipatively into the bottom of the total matter potential they are likely to steepen the underlying DM distribution simply through gravitational processes (Blumenthal et al. 1986). This situation would only exacerbate the difference between our observed shallow slopes and those expected from N-body simulations.

It has also been suggested by Loeb & Peebles (2003) that if stars form at high redshift ($z > 6$) before large structures form that they can be treated in a similar manner as the underlying DM particles. This scenario would suggest that instead of separating dark and luminous components of the matter distribution for comparison with simulations that we should compare the total mass distribution observed with the DM distribution found in N-body simulations. However, Loeb & Peebles (2003) admit that this scenario is not strongly motivated and that some dissipative process must still take place within the baryonic material. Recently, Dekel et al. (2003) have suggested that DM halos must be as cuspy as NFW due to the merger process, unless satellite halos are disrupted at large radii, possibly due to baryonic feedback. One final scenario describes a situation in which baryonic material is initially concentrated in small clumps of mass ($\geq 0.01\%$ of the total mass) with dynamical friction causing the final DM halo shape to flatten due to these clumps (El-Zant et al. 2003; El-Zant, Shlosman & Hoffman 2001). The issue of baryons must be looked into further and it is possible that the DM “core” problem cannot be resolved until baryonic material can be properly incorporated into the numerical experiments.

We have gone to great lengths in this paper to disentangle the luminous BCG component from the overall cluster DM in our mass model so that we could compare directly our results with those of N-body simulations. Albeit with considerable scatter, the average DM density profile is too shallow, especially if adiabatic contraction describes well the interaction between dark and baryonic matter. Does this indicate that something may be wrong with the Λ CDM paradigm of structure formation? Dark matter only simulations do not appear to be sufficient, especially as they begin to probe down to scales where complicated gaseous physics play a significant role. While work has been done to model the formation of cDs and BCGs (see e.g. Dubinski 1998; Nipoti et al. 2003) these have mainly focused on the accretion of galaxies to form cD-like objects, and have not been concerned with the resulting effect on the DM halo.

7.2. Is the DM slope universal?

This is a question that begs to be asked after looking at Figure 4. We detect an intrinsic scatter in β values of $\Delta\beta \sim 0.3$ in the radial arc sample. Unfortunately, the tangential arc sample can give only an upper limit on β , and thus does not provide any further measure of the scatter.

The most recent and highest resolution N-body simulations of eight galaxy clusters performed by Fukushige et al. (2003) did show some signs of run-to-run inner slope variations, and although they claimed that this argued against a “universal” inner DM profile, they did

not quantify the scatter. Several claims have been made that the DM density profile is dependent on the DM halo mass (e.g. Ricotti 2002; Jing & Suto 2000), however, these studies have focused on the difference in slopes between different mass scales (e.g. individual galaxies versus clusters of galaxies) while the clusters in this study are all roughly the same mass. It is plausible that the formation history of any given cluster sized halo can cause a natural cosmic scatter in β (e.g. Nusser & Sheth 1999). Ultimately, numerical simulations should be able to reproduce not only the observed mean slope of the DM density profile in galaxy clusters, but also its measured scatter.

8. Summary

We have performed a joint gravitational lensing and dynamical analysis in the inner regions of six galaxy clusters in order to constrain the inner DM density slope β . By studying the velocity dispersion profile of the BCG, we were able to disentangle luminous and DM components of the total matter distribution in these clusters on scales < 100 kpc. The main results of the paper can be summarized as follows:

1) The average inner slope of the 3 systems with both radial and tangential arcs is $\langle\beta\rangle = 0.52_{-0.05}^{+0.05}$. The 3 clusters with only tangential arcs provide an upper limit of $\beta < 0.57$ (99%CL). The measured slopes are thus inconsistent at high confidence level ($> 99\%$ CL) with the cusps ($\beta = 1 - 1.5$) predicted by dark matter only cosmological numerical simulations.

2) The agreement of the results from the radial arc sample and the tangential sample shows that the shallow slopes found for MS2137-23 (Sand et al. 2002) and the other radial arc systems are not the result of a selection effect.

3) Our precise measurements allow us to give a first estimate of the intrinsic scatter of the inner density DM slope ($\Delta\beta\sim 0.3$) of clusters of galaxies. The analysis of a larger sample of systems to better characterize the intrinsic scatter of the inner slope would provide a further observational test for future numerical simulations.

4) Our method is robust with respect to known systematic effects, including those related to the choice of the mass model, the description of orbital anisotropy in the dynamical models, and the simplifying assumptions inherent to our axisymmetric lensing analysis. A comprehensive and detailed analysis of these effects shows that the related systematic uncertainties on β are smaller than 0.2. Therefore, even for the system with the smallest random uncertainties (Abell 383) systematic errors do not dominate the error budget.

In conclusion, our results are in marked disagreement with the predictions of dark matter

only cosmological simulations. The inclusion of baryons in the models via a simple adiabatic contraction mechanism would further steepen the theoretical dark matter halo making the disagreement even more pronounced. Therefore, a more sophisticated treatment of baryons in the simulations appears necessary if one wants to reconcile the CDM paradigm with the present observations.

We would like to thank the referee for a thorough and constructive report. Also, we would like to acknowledge useful discussions with Neal Dalal, Chuck Keeton, Matthias Bartelmann and Massimo Meneghetti. We acknowledge financial support for proposal number HST-AR-09527 provided by NASA through a grant from STScI, which is operated by AURA, under NASA contract NAS5-26555. DJS would like to acknowledge financial support from NASA’s Graduate Student Research Program; NASA grant No. NAGT-50449. DJS is grateful for statistical advice given by Benjamin D. Wandelt. We are grateful for the use of the Gauss-Hermite Pixel Fitting Software developed by R.P. van der Marel. We thank Edo Berger, Alicia Soderberg and Shri Kulkarni for the NIRC observations. We would also like to thank Jean-Paul Kneib and Pieter van Dokkum for personally recommending clusters MACS 1206 and Abell 1201, respectively. We are grateful to the MACS collaboration, in particular Harald Ebeling, Alastair Edge and Jean-Paul Kneib, for access to MACS 1206. GPS thanks Jean-Paul Kneib for sharing his LENSTOOL ray tracing code. DJS would like to thank Melissa Enoch for providing CPU time. We would like to thank all those who have worked to make both LRIS and ESI such fantastic instruments. Finally, the authors wish to recognize and acknowledge the cultural role and reverence that the summit of Mauna Kea has always had within the indigenous Hawaiian community. We are most fortunate to have the opportunity to conduct observations from this mountain.

A. Analysis Technique

A.1. Lensing

Given our simple, spherically symmetric two-component mass model, we adopted a simple lensing analysis using only the positions and redshifts of the gravitational arcs in our sample. Our method is a generalization of that used by Bartelmann (1996).

Since the extent of the galaxy cluster (lens) is much less than the distance from the observer to the lens and the lens to the source, we make the thin-screen approximation in our gravitational lensing calculations. The total surface mass density is the sum of the luminous and DM components: $\Sigma_{tot} = \Sigma_{DM} + \Sigma_L$. The surface mass density of our chosen

DM halo profile, $\Sigma_{DM}(R)$, is

$$\Sigma_{DM}(R) = 2\rho_c r_{sc} \delta_c x^{1-\beta} \int_0^{\pi/2} d\theta \sin \theta (\sin \theta + x)^{\beta-3}, \quad (\text{A1})$$

where $x = R/r_{sc}$ (Wyithe, Turner & Spergel 2001). The surface mass density of the luminous component is $\Sigma_L = I(R)M_*/L$, where $I(R)$ is given in Jaffe’s (1983) original paper.

Using standard gravitational lensing nomenclature (see, e.g., Schneider, Ehlers, & Falco 1992) we describe Σ_{tot} in terms of the critical surface mass density, Σ_{cr} ,

$$\kappa(R) = \frac{\Sigma_{tot}(R)}{\Sigma_{cr}}, \quad (\text{A2})$$

where

$$\Sigma_{cr} = \frac{c^2}{4\pi G} \frac{D_s}{D_l D_{ls}}, \quad (\text{A3})$$

and D_l , D_{ls} , and D_s are the angular diameter distance to the lens, between the lens and source and to the source, respectively. Another convenient quantity when describing the mapping from the source plane to the lens plane is dimensionless and proportional to the mass inside projected radius x ,

$$m(x) = 2 \int_0^x dy \kappa(y) y. \quad (\text{A4})$$

With these definitions, the two eigenvalues of the Jacobian mapping between the source and image plane read:

$$\lambda_r = 1 - \frac{d}{dx} \frac{m(x)}{x}, \quad \lambda_t = 1 - \frac{m(x)}{x^2}. \quad (\text{A5})$$

The root of these two equations describes the radial and tangential critical curves of the lens. Since the magnification of the source is equal to the inverse of the determinant of the Jacobian, the radial and tangential critical curves are where the magnification of the source formally diverges. While this does not happen in practice (due to the spatial extent of the source), it guarantees that when an image of a source lies near a critical line it is strongly distorted (in the radial direction in the case of radial arcs and tangentially for the case of tangential arcs). Merging lensed images merge across critical lines, which provides a simple way of approximating their position by visual inspection. Thus highly distorted image pairs are an excellent way of approximating the position of the critical line for a lens. For the simple, axisymmetric lens model explored in this work, both the radial and

tangential critical lines are circular with the radial critical curve always lying inside that of the tangential critical curve. Our sample of clusters (approximately round clusters with little visible substructure) was chosen specifically with this concern in mind (tests of our lens model are described in § 6.1). However, this is not always the case. Therefore, extreme caution must be exercised when applying our simple lens model to other samples of clusters.

Given our mass model (§5.1), the measured redshifts of the arcs and clusters, and a set of free parameters $\{M_*/L, \beta, \delta_c\}$, we can compute the predicted position of the arcs (assuming they lie very close to their associated critical line), by finding the root of the appropriate eigenvalue from Eq. A5. By comparing the predicted position of the arcs with the actual position taken from the images, we can calculate the likelihood function,

$$P(M_*/L, \delta_c, \beta) \propto \exp\left\{-\frac{1}{2}\sum_i \left[\frac{y_i - \tilde{y}_i(M_*/L, \delta_c, \beta)}{\Delta_i}\right]^2\right\}, \quad (\text{A6})$$

assuming that our underlying distributions are normal. Here, y is the distance of the arc from the center of the cluster potential (as measured from the center of the BCG), Δ_i is our assigned uncertainty to the position of the critical line and the sum in the exponential is over all the critical line arcs with known redshift.

A.2. Dynamics

In addition to the gravitational arc redshifts, we have also measured extended velocity dispersion profiles for all of the BCGs in our sample. This is used as an additional constraint on our mass model, using a joint likelihood analysis.

We compute the model velocity dispersion starting from the spherical Jeans Equation (Binney & Tremaine 1987):

$$\frac{d\rho_*(r)\sigma_r^2(r)}{dr} + \frac{2\alpha(r)\rho_*(r)\sigma_r^2(r)}{r} = -\frac{GM_{enc}(r)\rho_*(r)}{r^2}, \quad (\text{A7})$$

where G is Newton’s gravitational constant, $M(r)$ is the three-dimensional mass enclosed, σ_r is the radial velocity dispersion. The anisotropy parameter $\alpha(r)$ is defined as,

$$\alpha(r) \equiv 1 - \frac{\sigma_\theta^2(r)}{\sigma_r^2(r)} \equiv \frac{r^2}{r^2 + r_a^2}, \quad (\text{A8})$$

where σ_θ is the tangential component of the velocity dispersion. The final definition introduces the Osipkov-Merritt (Osipkov 1979; Merritt 1985a,b) parameterization of anisotropy that we mainly use in our dynamical models. By default, we use isotropic orbits (i.e $r_a = \infty$)

which appears to be a realistic description of the inner regions of early-type galaxies. However, in §6.2 we explore the consequences of anisotropic velocity dispersion tensors on DM density profiles we measure, by considering $r_a \geq 0$ models and models with constant tangential anisotropy ($\alpha < 0$).

Using our parameterization of the anisotropy, we can readily derive the radial velocity dispersion (Binney 1980)

$$\sigma_r^2(r) = \frac{G \int_r^\infty dr' \rho_*(r') M_{enc}(r') \frac{r_a^2 + r'^2}{r'^2}}{(r_a^2 + r^2) \rho_*(r)} \quad (\text{A9})$$

and the projected velocity dispersion

$$\sigma_p^2(R) = \frac{2}{(M_*/L)I(R)} \int_R^\infty dr' \left[1 - \frac{R^2}{r_a^2 + r'^2} \right] \frac{\rho_*(r') \sigma_r^2(r') r'}{(r'^2 - R^2)^{1/2}}, \quad (\text{A10})$$

with $I(R)$ being the surface brightness profile (modeled as a Jaffe profile with parameters derived from surface photometry).

Before comparing the model with the observations it is necessary to take two further steps. First, we must account for the atmospheric seeing, which blurs spectroscopic measurements in the spatial direction. This can be modeled as:

$$\sigma_s^2(R) = \frac{\int d^2R' P(R - R') I(R') \sigma_p^2(R')}{\int d^2R' P(R - R') I(R')} \quad (\text{A11})$$

where we assume a Gaussian point-spread function, $P(R-R')$ (see discussion in Binney & Merrifield 1998; Eqn. 4.6-4.8).

Second, we must account for the non negligible slit width and spatial binning used. This was calculated numerically such that,

$$\sigma_b^2(R) = \frac{\int_A dA' I_s(R') \sigma_s^2(R')}{\int_A dA' I_s(R)}, \quad (\text{A12})$$

where A is the area of the slit used for a given measurement and $I_s(R)$ is the seeing corrected intensity at a given projected radius.

With an understanding of the observational setup and seeing conditions one can calculate the expected velocity dispersion for a given set of free parameters, $\{M_*/L, \beta, \delta_c\}$. Analogous to the likelihood technique employed in the lensing appendix subsection, one can construct a likelihood for the velocity dispersion profile of the BCGs by comparing the

expected velocity dispersion for a given set of free parameters with the measured velocity dispersion,

$$P(M_*/L, \delta_c, \beta) \propto \exp\left\{-\frac{1}{2}\sum_i \left[\frac{\sigma_i - \tilde{\sigma}_i(M_*/L, \delta_c, \beta)}{\Delta_i}\right]^2\right\}. \quad (\text{A13})$$

Here, σ is the velocity dispersion in a given bin and Δ_i is the uncertainty in the measurement.

With both the lensing and velocity dispersion likelihoods calculated, it is now possible to find constraints on the inner dark matter density slope, β . Since the two techniques are independent, the total likelihood for a given set of free parameters is just the product of the lensing and velocity dispersion likelihoods.

REFERENCES

- Arabadjis, J. S., Bautz, M. W., Arabadjis, G. 2003, astro-ph/0305547
- Arabadjis, J. S., Bautz, M. W., Garmire, G. P. 2002, ApJ, 572, 66
- Allen, S. W., Schmidt, R. W., & Fabian, A. C. 2002, MNRAS, 335, 256
- Bahcall, N. A. et al. 2003, ApJ, 585, 182
- Bartelmann, M. 1996, A&A, 313, 697
- Binney, J., & Merrifield, M. 1998, Galactic Astronomy, Princeton University Press, Princeton
- Binney, J. & Tremaine, S, 1987, Galactic Dynamics, Princeton University Press, Princeton
- Binney, J. 1980, MNRAS, 190, 873
- Blumenthal, G. R., Faber, S. M., Flores, R., & Primack, J. R. 1986, ApJ, 301, 27
- Borriello, A., Salucci, P., 2001, MNRAS, 323, 285
- Borriello, A., Salucci, P., Danese, L. 2003, MNRAS, 341, 1109
- Bullock, J. S., Kolatt T. S., Sigad, Y., Somerville, R. S., Kravtsov, A. V., Klypin, A. A., Primack, J. R., & Dekel, A. 2001, MNRAS, 321, 598
- Cardelli J., Clayton, G., & Mathis, J., 1989, ApJ, 345, 245
- Croft, R. A. C. et al. 2002, ApJ, 581, 20

- Dahle, H., Hannestad, S., Sommer-Larsen, J., 2003, *ApJ*, 588, 73
- de Blok, W. J. G., McGaugh, S. S., Bosma, A., & Rubin, V. C. 2001, *ApJ*, 552, 23
- de Blok, W. J. G., & Bosma, A. 2002, *A&A*, 385, 816
- Dubinski, J. 1998, *ApJ*, 502, 141
- Edge, A. C., Smith, G. P., Sand, D. J., Treu, T., Ebeling, H., Allen, S. W., van Dokkum, P. G. 2003, *ApJ* in press astro-ph/0311205
- Ellis, R., Allington-Smith, J., Smail, I. 1992, *MNRAS*, 249, 184
- El-Zant, A., Shlosman, I., Hoffman, Y. 2001, *ApJ*, 560, 636
- El-Zant, A., Hoffman, Y., Primack, J., Combes, F. & Shlosman, I., 2003, *ApJL* submitted, astro-ph/0309412
- Ettori, S., Fabian, A. C., Allen, S.W., & Johnstone, R.M., 2002, *MNRAS*, 331, 635
- Fisher, D., Illingworth, G., Franx, M. 1995, *ApJ*, 438, 539
- Fort, B., Le Fevre, O., Hammer, F., & Cailloux, M. 1992, *ApJ*, 399, L125
- Franx, M. 1993, *PASP*, 105, 1058
- Frenk, C. S. 2002, astro-ph/0208219
- Fruchter, A. S., & Hook, R. N. 2002, *PASP*, 114, 14
- Fukushige, T., Kawai, A., Makino, J. 2003, *ApJ* submitted, (astro-ph/0306203)
- Gavazzi, R., Fort, B., Mellier, Y., Pelló, R., Dantel-Fort, M. 2003, *A&A*, 403, 11
- Gebhardt, K. et al. 2003, *ApJ*, 583, 92
- Gerhard, O., Kronawitter, A., Saglia, R. P., & Bender, R. 2001, *AJ*, 121, 1936
- Ghigna, S., Moore, B., Governato, F., Lake, G., Quinn, T., & Stadel, J. 2000, *ApJ*, 544, 616
- Hammer, F., Gioia, I., Shaya, E., Teyssandier, P., Le Fevre, O., & Luppino, G. 1997, *ApJ*, 491, 477 Hattori, M., Kneib, J. -P., & Makino, N. 1999, *Prog. Theor. Phys. Suppl.*, 133 1
- Hernquist, L. 1990, *ApJ*, 356, 359

- Jaffe, W. 1983, MNRAS, 202, 995
- Jimenez, R., Verde, L., & Oh, S. P. 2002, MNRAS, 339, 243
- Jing, Y. P., Suto, Y. 2000, ApJ, 529, L69
- Jones, C., Mandel, E., Schwarz, J., Forman, W., Murray, S. S., & Harnden, F. R. 1979, ApJ, 234, L21
- Jorgensen, I., Franx, M., Kjaergaard, P. 1995, MNRAS, 276, 1341
- Kassiola, A., & Kovner, I. 1993, ApJ, 417, 450
- Kelson, D., Zabludoff, A., Williams, K., Trager, S., Mulchaey, J., & Bolte, M. 2002, ApJ, 576, 720
- Kelson, D., Illingworth, G. D., van Dokkum, P. G., & Franx, M. 2000, ApJ, 531, 159
- Klypin, A., Kravtsov, A. V., Bullock, J. S., Primack, J. R. 2001, ApJ, 554, 903
- Kneib, J.-P. 1993, Ph.D. thesis, Univ. Paul Sabatier, Toulouse, France
- Kneib, J.-P., Ellis, R. S., Smail, I., Couch, W. J., & Sharples, R. M. 1996, ApJ, 471, 643
- Kneib, J.-P., et al., 2003 ApJ, submitted, astro-ph/0307299
- Koopmans, L. V. E., & Treu, T. 2003, ApJ, 583, 606
- Koopmans, L. V. E., Treu, T., Fassnacht, C. D., Blandford, R. D., & Surpi, G. 2003, ApJ, accepted, astro-ph/0306216
- Krist, J., 1993, in ASP Conf. Ser. 52, Astronomical Data Analysis Software and Systems II, ed. R. J. Hanisch, R. J. V. Brissenden, and J. Barnes (San Francisco: ASP), 536
- Kronawitter, A., Saglia, R.P., Gerhard, O., & Bender, R. 2000, A&AS, 144, 53
- Landolt, A. U. 1992, AJ, 104, 340
- Laine, S., van der Marel, R. P., Lauer, T. R., Postman, M., O’Dea, C. P., Owen, F.N. 2003, AJ, 125, 478
- Lewis, A. D., Buote, D. A., Stocke, J. T., 2003, ApJ, 586, 135L
- Loeb, A., Peebles, P. J. E. 2003, ApJ, 589, L29
- Mellier, Y., Fort, B., & Kneib, J.-P. 1993, ApJ, 407, 33

- Merritt, D., & Aguilar, L. A. 1985, MNRAS, 217, 787
- Miralda-Escudé, J. 1995, ApJ, 438, 514
- Miralda-Escudé, J. 2002, ApJ, 564, 60
- Moore, B., Governato, F., Quinn, T., Stadel, J. & Lake, G. 1998, ApJ, 499, L5 (Moore)
- Natarajan, P., Kneib, J.-P. 1996, MNRAS, 283, 1031
- Navarro, J., Frenk, C. S., & White S. D. M 1997, ApJ, 490, 493 (NFW97)
- Nipoti, C., Stiavelli, M., Ciotti, L., Treu, T., & Rosati, P. 2003, MNRAS, accepted, astro-ph/0306082
- Nusser, A. & Sheth, R. K. 1999, MNRAS, 303, 685
- Oke, J. B. et al. 1995, PASP, 107, 375
- Osipkov, L. .P. 1979, Pis'ma Astron. Zh., 5, 77
- Pratt, G. W., Arnaud, M. 2002, A&A, 394, 375
- Percival, W. J. et al. 2001, MNRAS, 327, 1297
- Power, C., Navarro, J. F., Jenkins, A., Frenk, C. S., White, S. D. M., Springel, V., Stadel, J., & Quinn, T. 2003, MNRAS, 338, L14
- Ricotti, M. 2002, MNRAS, accepted, astro-ph/0212146
- Sand, D. J., Treu, T., & Ellis, R. S. 2002, ApJ, 574, L129 (STE02)
- Schmidt, R. W., Allen, S. W., & Fabian, A. C. 2001, MNRAS, 327, 1057
- Schneider, P., Ehlers, J. & Falco, E. E. 1992, Gravitational Lenses, Springer-Verlag, Berlin.
- Schlegel, D. J., Finkbeiner, D. P., & Davis, M. 2000, ApJ, 500, 525
- Sheinis, A. I., et al. 2002, PASP, 114, 851
- Simon, J. D., Bolatto, A. D., Leroy, A., Blitz, L., 2003, ApJaccepted, astro-ph/0307154
- Smith, G. P., Kneib, J.-P., Ebeling, H., Czoske, O., & Smail, I. R. 2001, ApJ, 552, 493
- Smith, G. P. 2002, Ph. D. thesis, Univ. of Durham, UK, available upon request from gps@astro.caltech.edu

- Spergel, D. N. et al. 2003, ApJ, in press, astro-ph/0302209
- Stiavelli, M., & Sparke, L. 1991, ApJ, 382, 466
- Swaters, R. A., Madore, B. F., van den Bosch, F. C., & Balcells, M., 2003, ApJ, 583, 732
- Tasitomi, A., Kravtsov, A. V., Gottloeber, S., Klypin, A. A. 2003, ApJsubmitted, astro-ph/0311062
- Treu, T., Stiavelli, M., Møller, P.M., Casertano, C., & Møller, & P.M., Bertin G., 2001, MNRAS, 326, 221
- Treu, T., Stiavelli, M., Casertano, C., Møller, P., & Bertin G. 1999, MNRAS, 308, 1307
- Treu, T., Stiavelli, M., Bertin G., Casertano, C., & Møller, P. 2001, MNRAS, 326, 237
- Treu, T., Stiavelli, M., Casertano, C., Møller, P., & Bertin, G. 2002, ApJ, 564, L13
- Treu, T., Koopmans, L. V. E., 2002, ApJ, 575, 87
- Tyson, A., Kochanski, G., & dell’Antonio, I., 1998, ApJ, 498, L107
- van Albada, T.S. 1982, MNRAS, 201, 939
- van den Bosch, F. C. & Swaters, R. A. 2001, MNRAS, 325, 1017
- van der Marel, R. P. 1994, MNRAS, 270, 271
- van der Marel, R. P., Magorrian, J., Carlberg, R. G., Yee, H. K. C., & Ellingson, E. 2000, AJ, 119, 2038
- van Dokkum, P. G., Franx, M. 1996, MNRAS, 281, 985
- van Dokkum, P. G. 2001, PASP, 113, 142
- van Dokkum, P. G., Ellis, R. S. 2003, PASP, 592, L53
- Williams, L., Navarro, J., & Bartelmann, M. 1999, ApJ, 527, 535
- Wu, X. 2000, MNRAS, 316, 299
- Wyithe, J. S.B., Turner, E. L., Spergel, D. N. 2001, ApJ, 555, 504

Table 1: Optical/NIR Imaging Log

Cluster	z_{clus}	Date	Telescope/ Instrument	Filter	Exposure time (ks)
MS2137-23	0.313	May 28-31,1995	HST/WFPC2	F702W	22.2
Abell 383	0.189	Jan 25, 2000	HST/WFPC2	F702W	7.5
		Dec 17, 2002	Keck/NIRC	K_s	1.0
Abell 963	0.206	May 7, 2000	HST/WFPC2	F702W	7.8
RXJ 1133	0.394 ^a	Feb 20, 2001	HST/WFPC2	F606W	1.0
		Dec 17, 2002	Keck/NIRC	K_s	0.8
MACS 1206	0.440 ^a	April 13, 2002	Keck/ESI	I	0.3
Abell 1201	0.169	April 7, 2001	HST/WFPC2	F606W	0.8

Note. — Imaging Observation Log of the clusters in our sample.

^aNew spectroscopic measurement

Table 2: BCG Photometric Properties

Cluster	Filter	R_e (arcsec/kpc)	M (mag)	SB_e (mag arcsec ⁻²)	K-color Correction	$(1 - b/a)_e$
MACS 1206	gunn I	2.08 ± 0.17	17.48 ± 0.07	22.46 ± 0.23	0.81 ± 0.03	0.35 ± 0.05
	V	12.75 ± 1.04	-23.93 ± 0.08	21.57 ± 0.23		
MS 2137-23	F702W	5.02 ± 0.50	16.48 ± 0.07	23.58 ± 0.34	0.49 ± 0.03	0.17 ± 0.01
	V	24.80 ± 1.68	-24.38 ± 0.09	22.76 ± 0.34		
RXJ 1133	F606W	5.18 ± 0.12	18.00 ± 0.06	24.96 ± 0.33	0.41 ± 0.03	0.18 ± 0.05
	B	29.73 ± 0.69	-23.44 ± 0.07	23.89 ± 0.33		
Abell 383	F702W	13.75 ± 0.60	14.67 ± 0.06	22.95 ± 0.25	0.60 ± 0.04	0.19 ± 0.03
	V	46.75 ± 2.04	-24.78 ± 0.07	22.72 ± 0.25		
Abell 1201	F606W	15.01 ± 0.10	15.44 ± 0.08	24.81 ± 0.21	0.10 ± 0.05	0.32 ± 0.02
	V	46.68 ± 0.31	-24.23 ± 0.09	24.18 ± 0.21		
Abell 963	F702W	11.04 ± 0.14	15.08 ± 0.05	23.67 ± 0.27	0.59 ± 0.03	0.36 ± 0.02
	V	40.19 ± 0.51	-24.38 ± 0.06	23.39 ± 0.27		

Note. — Photometric properties derived from our 2D surface brightness profile fitting. The first line for each cluster is in the observed filter while the second is in a rest filter. The K-color correction and ellipticity at the effective radius are listed as well.

Table 3: Gravitational Arc Properties

Cluster	R_{rad} (arcsec)	R_{tan} (arcsec)	z_{radial}	z_{tan}
MACS 1206	-	21.3 ± 0.4	-	1.035^a
MS 2137-23	4.5 ± 0.3	15.35 ± 0.20	1.502^b	1.501^b
RXJ 1133	3.2 ± 0.5	10.9 ± 0.3	1.544^a	1.544^a
Abell 383	1.90 ± 0.6	15.7 ± 0.4	1.010^a	1.009^a
Abell 1201	-	2.2 ± 0.3	-	0.451^c
Abell 963	-	11.9 ± 0.2	-	0.77^d

^aNew spectroscopic measurement

^bSand et al. 2002

^cEdge et al. 2003

^dEllis, Allington-Smith & Smail 1991

Note. — Geometric properties of the gravitational arcs and BCGs, along with the distance scale for each cluster based on the adopted cosmology. The BCG ellipticity at approximately the effective radius, R_e , and the positions of the gravitational arcs with respect to the BCG center are listed.

Table 4: Spectroscopic Observation Log

Cluster	Date	Target	Instrument	Exposure time (ks)	Seeing ($''$)	Pos. Angle (degrees)	Slit size ($''$)
MS2137-23	July 21,2001	Arcs/BCG	ESI	5.9	0.6	0	1.25
Abell 383	Dec 12, 2002	Rad. Arc/BCG	ESI	5.4	0.7	28	1.25
	Oct 19, 2001	Tan. Arc	LRIS	3.8	0.7	30	1.0
RXJ 1133	Apr 11-12, 2002	BCG/Rad. Arc	ESI	12.6	0.6-0.7	-24	1.25
	Apr 11, 2002	Tan Arc	ESI	3.6	0.7	10	1.25
MACS 1206	Apr 13, 2002	BCG	ESI	9.0	0.75	98	1.25
	Apr 13, 2002	Tangential arc	ESI	3.6	0.75	273	1.25
Abell 1201	Apr 12, 2002	BCG/tan arc	ESI	3.6	0.6	-32	1.25
Abell 1201	Apr 12, 2002	BCG/tan arc	ESI	3.6	0.6	-25	1.25
Abell 963	Mar 28, 2001	BCG	LRIS	4.8	0.7	-15.5	1.5

Note. — Summary of the spectroscopic observations.

Cluster	Spatial Binning (arcsec)	σ (km s ⁻¹)
MACS 1206	-0.30 - 0.30	257 ± 39
	0.30 - 1.37	245 ± 50
	-0.30 - -1.37	259 ± 52
RXJ 1133	0.0 - 0.61	333 ± 30
	0.61 - 1.22	306 ± 41
	1.22 - 1.98	337 ± 67
Abell 1201 PA=-32	-0.35 - 0.35	231 ± 13
	-1.06 - -0.35	257 ± 21
	0.35 - 1.06	232 ± 18
Abell 1201 PA=-25	1.06 - 1.76	224 ± 28
	-0.28 - 0.28	238 ± 16
	-0.99 - -0.28	252 ± 20
Abell 383	0.28 - 0.99	223 ± 15
	0.99 - 1.69	207 ± 20
	-0.49 - 0.07	319 ± 26
Abell 963	-1.06 - -0.49	228 ± 25
	-1.62 - -1.06	246 ± 32
	-0.32 - 0.32	299 ± 22
	-0.97 - -0.32	298 ± 29
	-1.61 - -0.97	271 ± 31
	0.32 - 0.97	282 ± 26
	0.97 - 1.61	253 ± 26

Table 5.— Velocity Dispersion Profiles. Tabulated velocity dispersion profiles of the BCGs, not including MS 2137-23, which was presented in STE02. All slit widths are 1''25 except for Abell 963, which is 1''50. All spatial values are with respect to the center of the BCG.

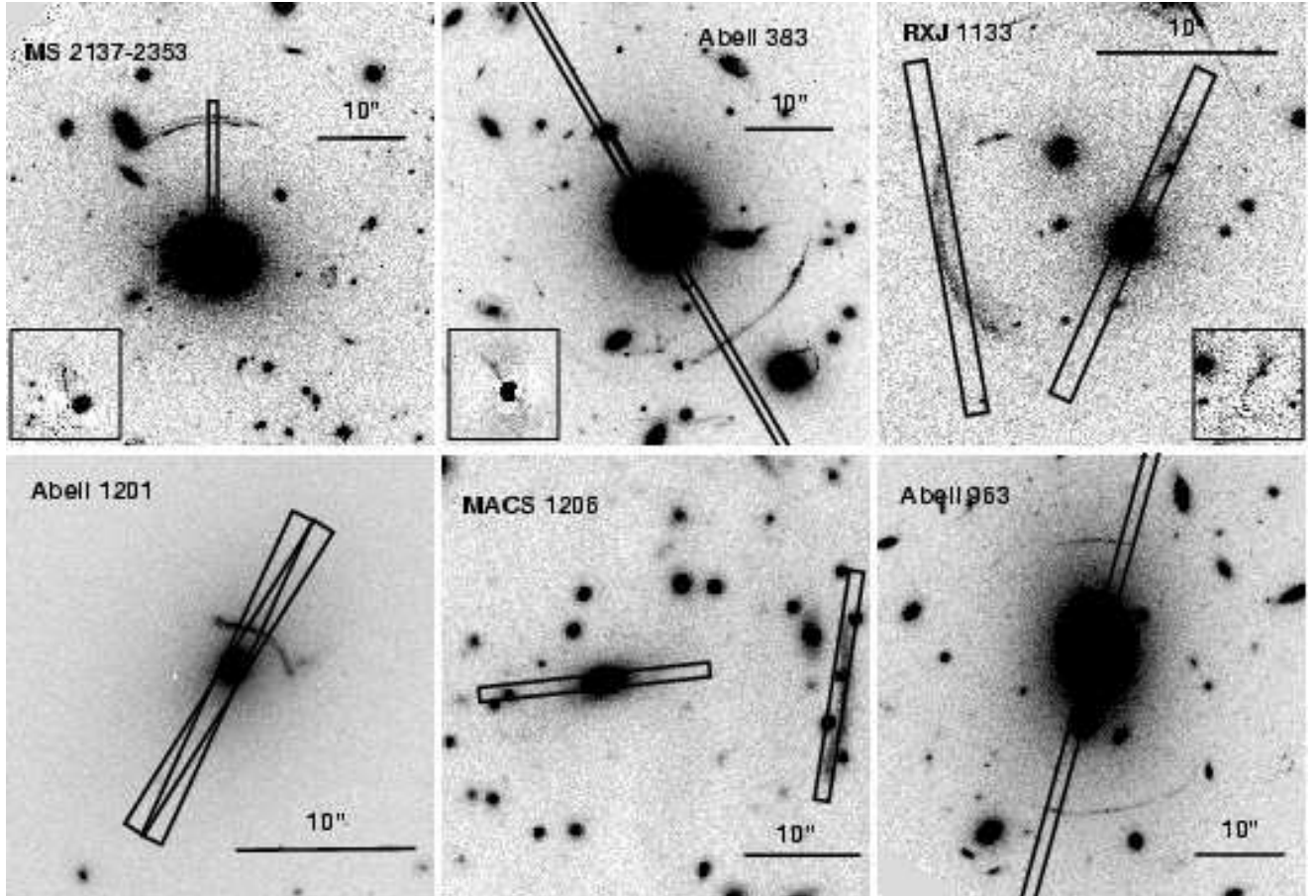


Fig. 1.— Images of the six clusters in this study. The top row features the clusters with both radial and tangential arcs. The postage stamp insets show zoomed in BCG subtracted images so that the radial arcs can be clearly seen. The bottom row contains those clusters with tangential arcs only. The overlaid “slits” correspond to the actual slit positions and sizes that were observed. See Table 4 for the spectroscopic observation log. North is up and East is to the left in all images.

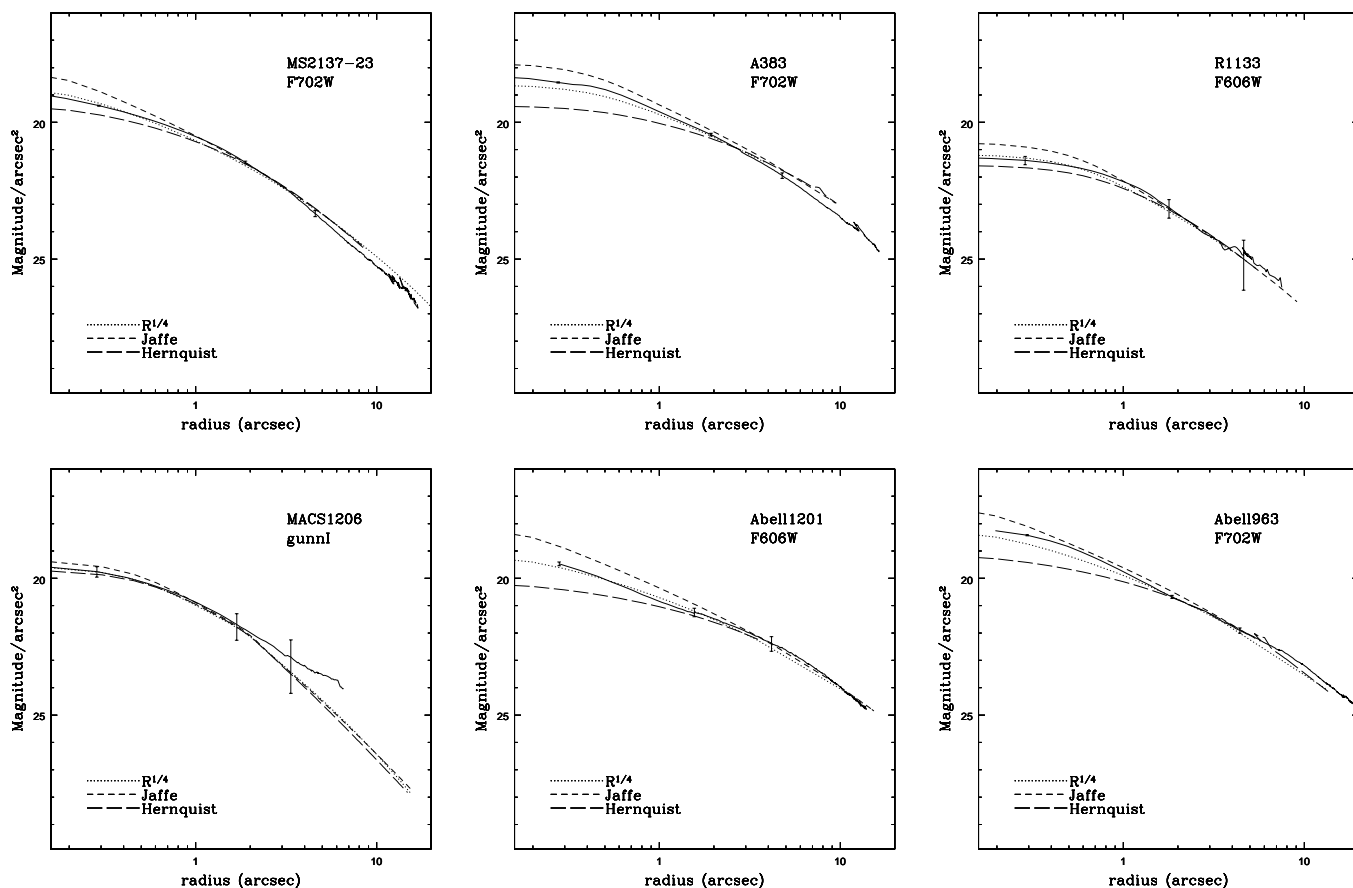


Fig. 2.— Surface brightness profile of the BCGs. The solid lines are the measured surface brightness profiles while the other curves are various parameterizations of the data based on a $r^{1/4}$ fit, convolved with the PSF of the observation. The uncertainty of the profile is given at several representative points. As can be seen, the Jaffe and Hernquist profile generally bracket the best-fitting $r^{1/4}$ at low radii. See §6.3 for a discussion of the effects our chosen luminous mass component parameterization has on our results.

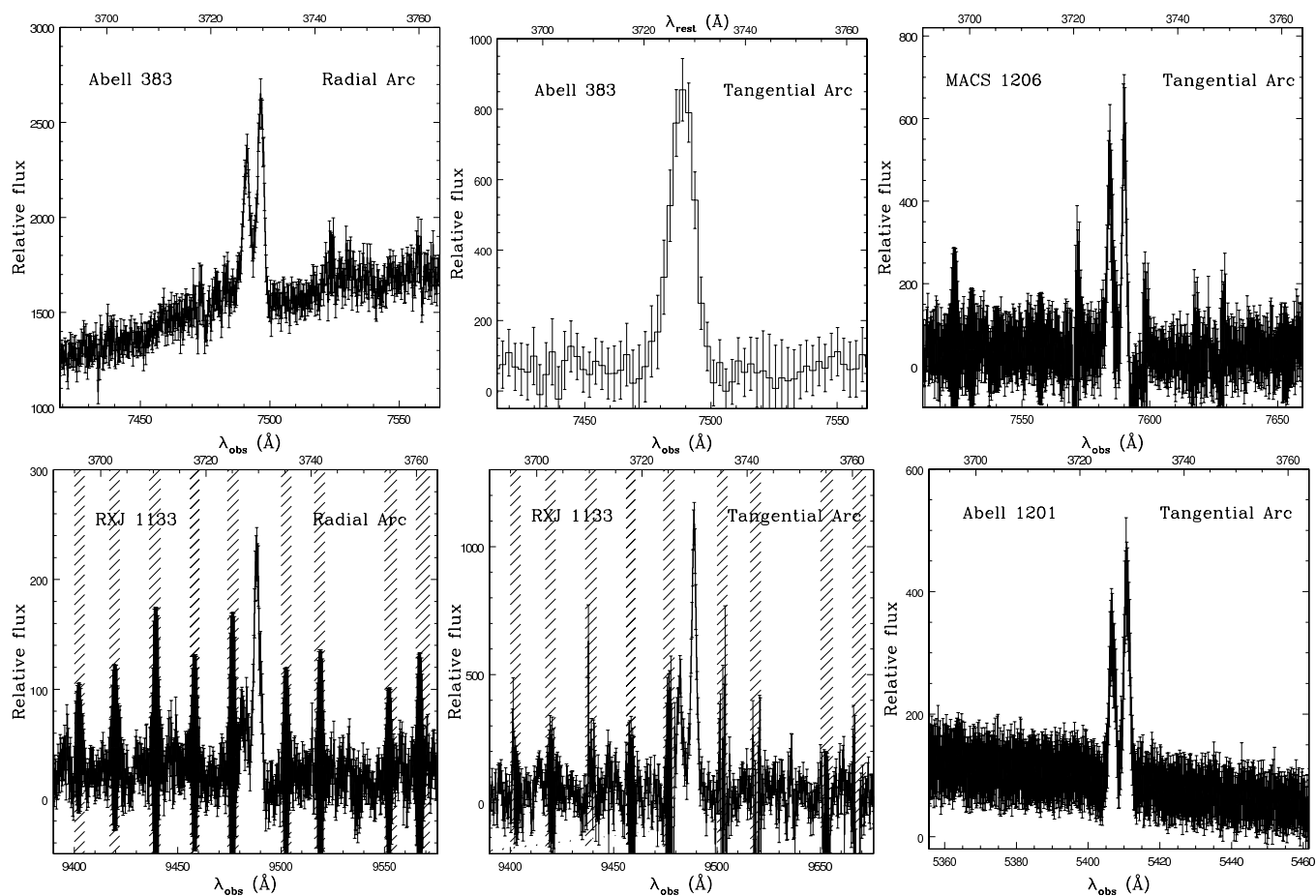


Fig. 3.— New gravitational arc redshift measurements. All new redshift measurements of gravitational arcs in this work were identified by strong [O II] in emission. Both the radial arc in Abell 383 and the tangential arc in Abell 1201 have strong continuum due to the nearby presence of the BCG. See Table 3 for a list of all gravitational arc redshift measurements used in this study.

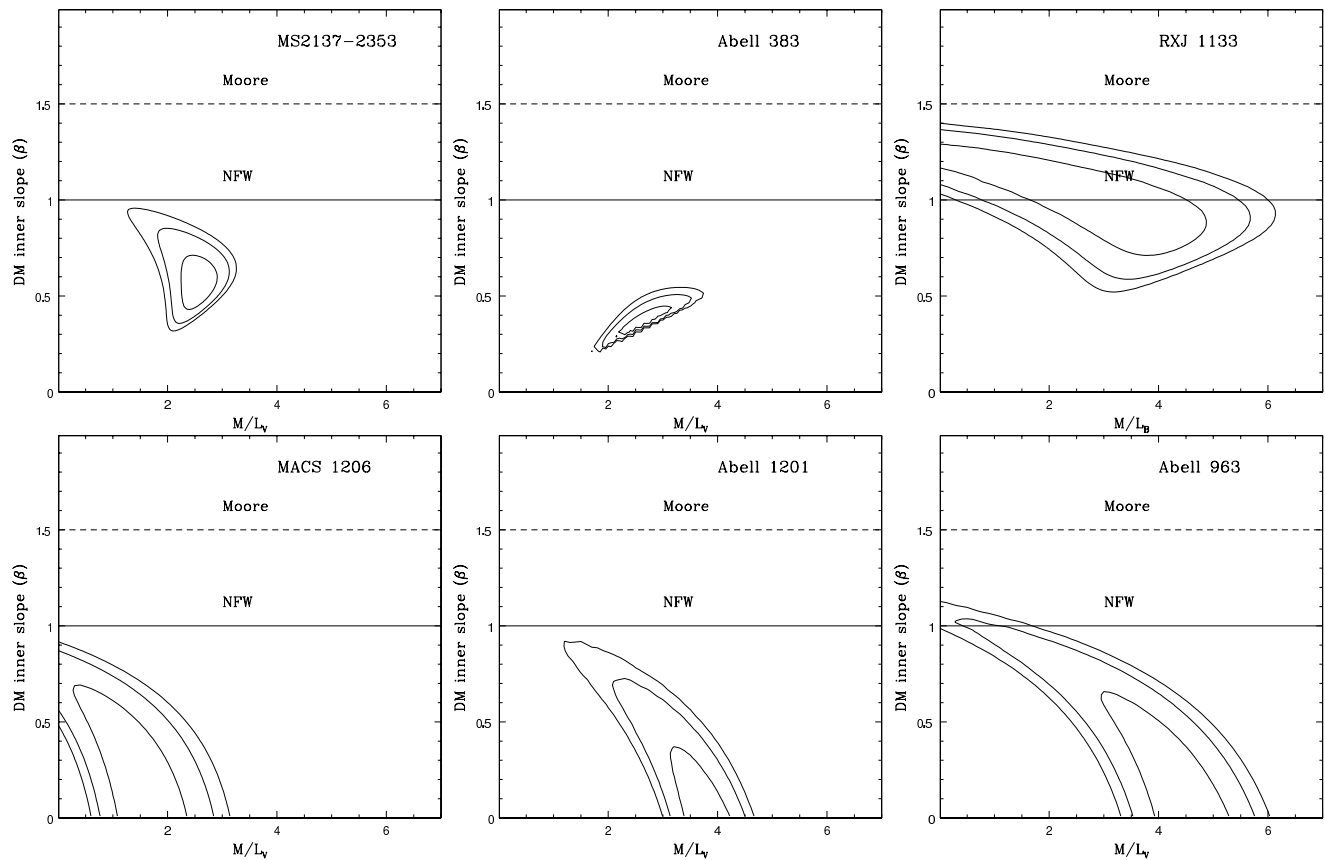


Fig. 4.— Likelihood contours (68%, 95% and 99%) obtained for the radial arc sample (top row) and the tangential arc sample (bottom row) with a Jaffe luminous distribution plus a generalized NFW DM distribution. These contours were obtained after both the lensing and dynamical analysis and marginalization with respect to δ_c .

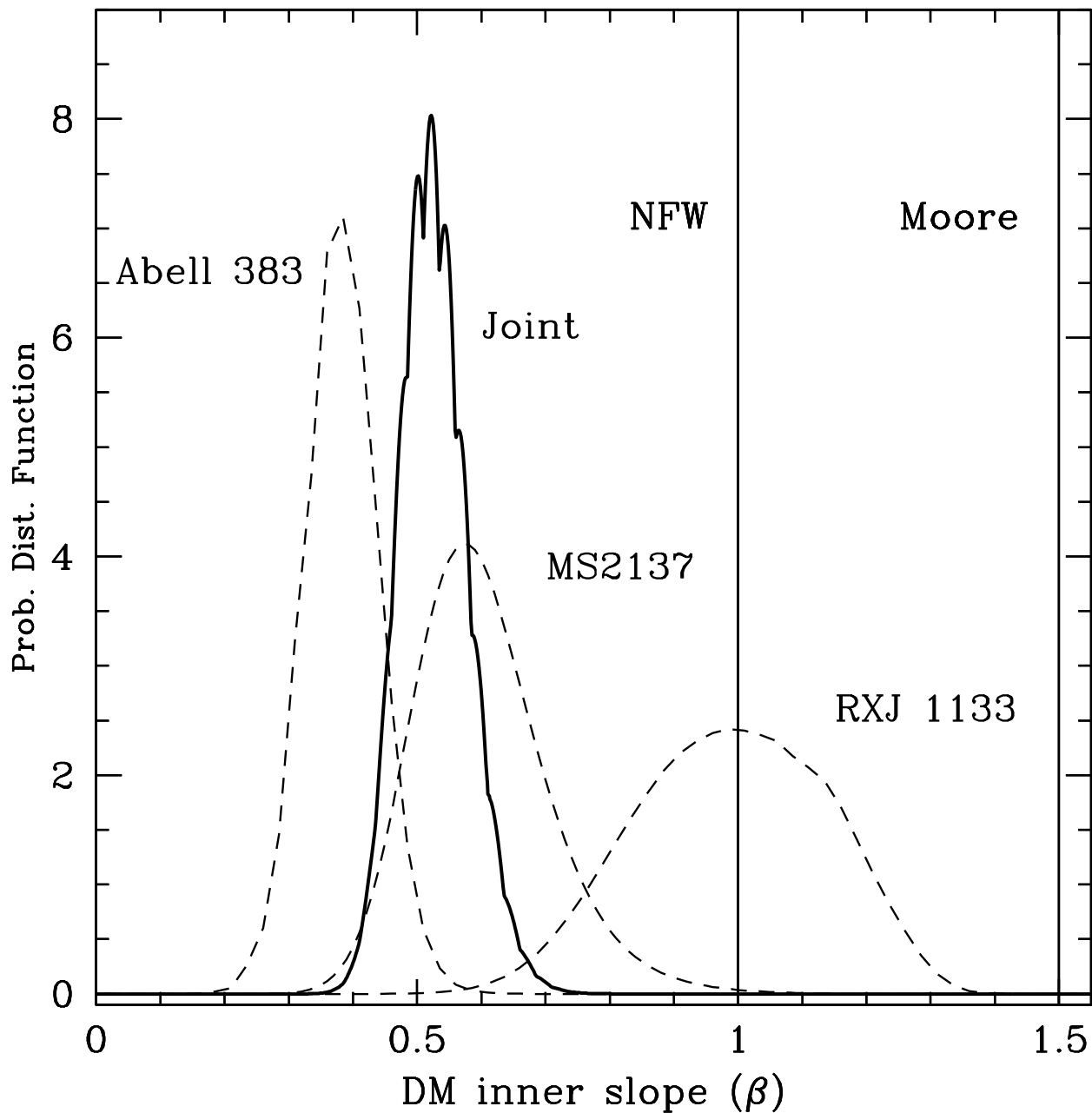


Fig. 5.— Probability distribution function of the DM inner density slope, β , for the three radial arc clusters. Note the wide scatter in preferred values of β from cluster to cluster, $\Delta\beta \sim 0.3$. The joint distribution was obtained by multiplying the individual PDFs and normalizing.

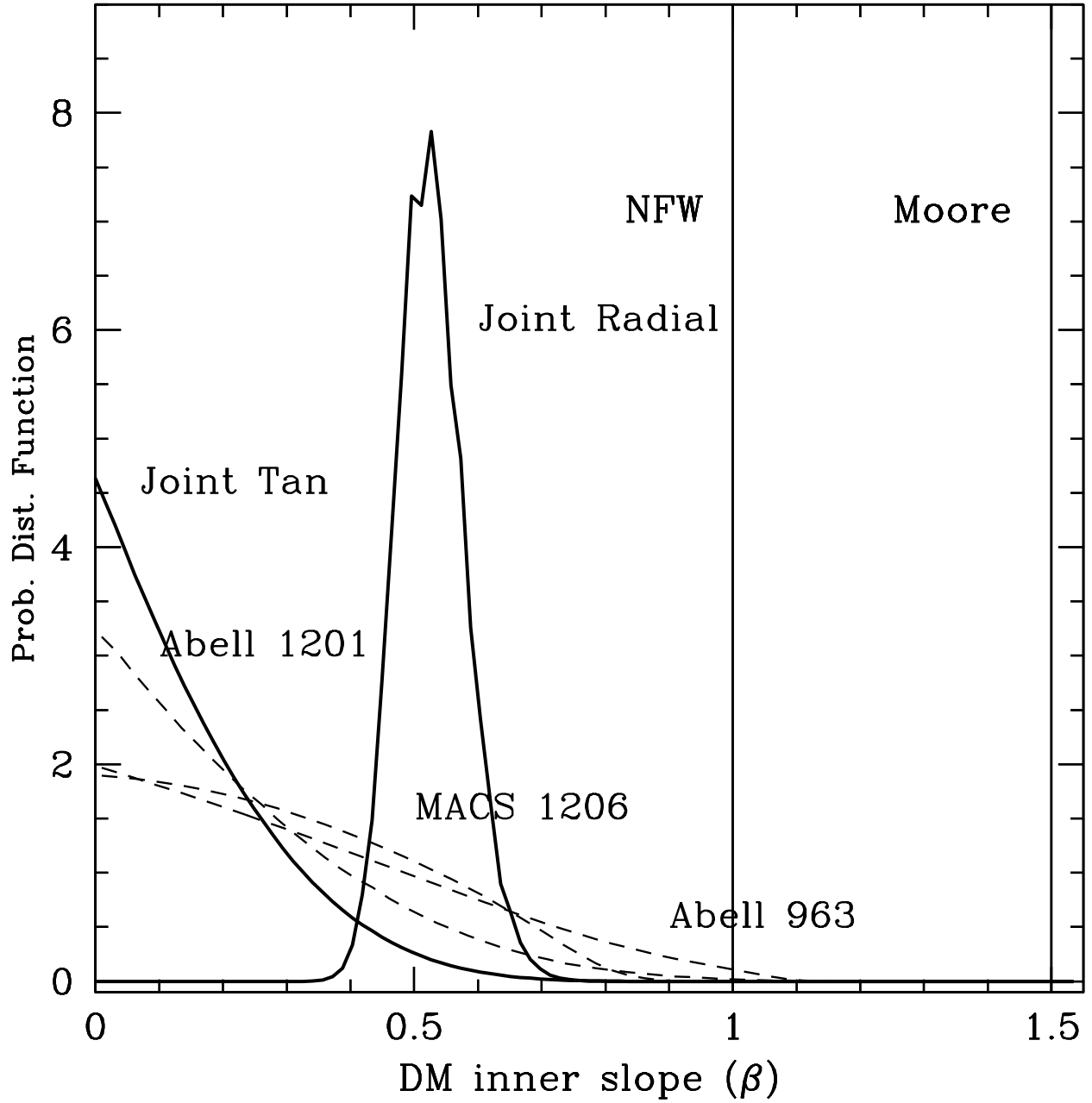


Fig. 6.— Probability distribution function of the DM inner density slope, β , for the tangential arc sample. These effectively allow us to place an upper limit on β for each cluster. Also plotted is the joint PDF for the radial arc sample and the tangential arc sample. There is no evidence that the radial arc sample is biased towards lower values of β .

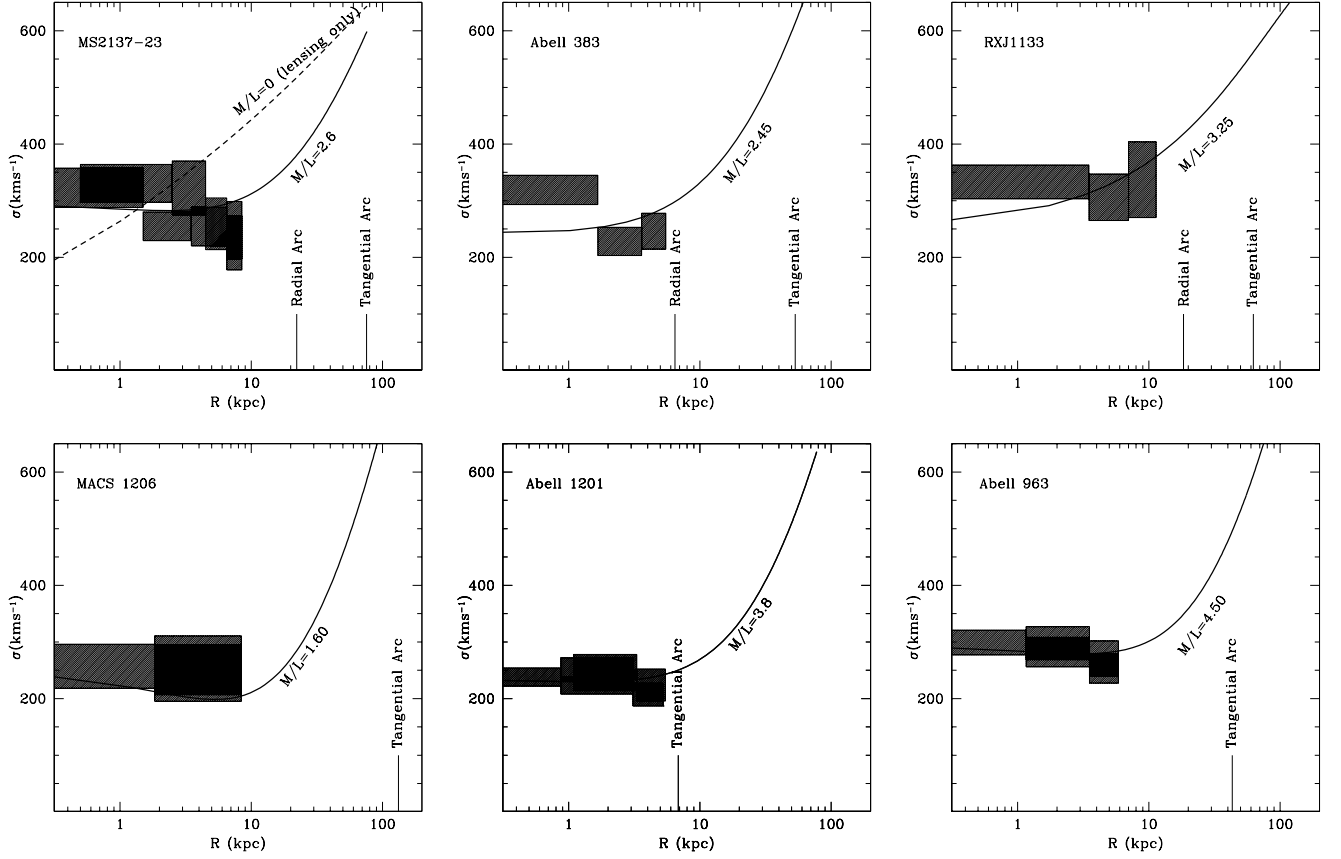


Fig. 7.— The measured velocity dispersion profile for each BCG (hatched boxes) along with the best-fitting velocity dispersion profile calculated from the combined lensing + dynamics analysis (solid curves). Note that the solid curves are not exactly equivalent to those derived from the analysis since they were not binned in accordance with the slit width, spatial binning of the measurement or smeared due to the effects of seeing. The plot of MS2137-23 (top left) illustrates the power of including the velocity dispersion profile of the BCG into our analysis. In this panel we have also shown a velocity dispersion profile from a mass model that is compatible with the lensing analysis of that cluster, but does not fit the velocity dispersion profile ($\beta=1.30$).

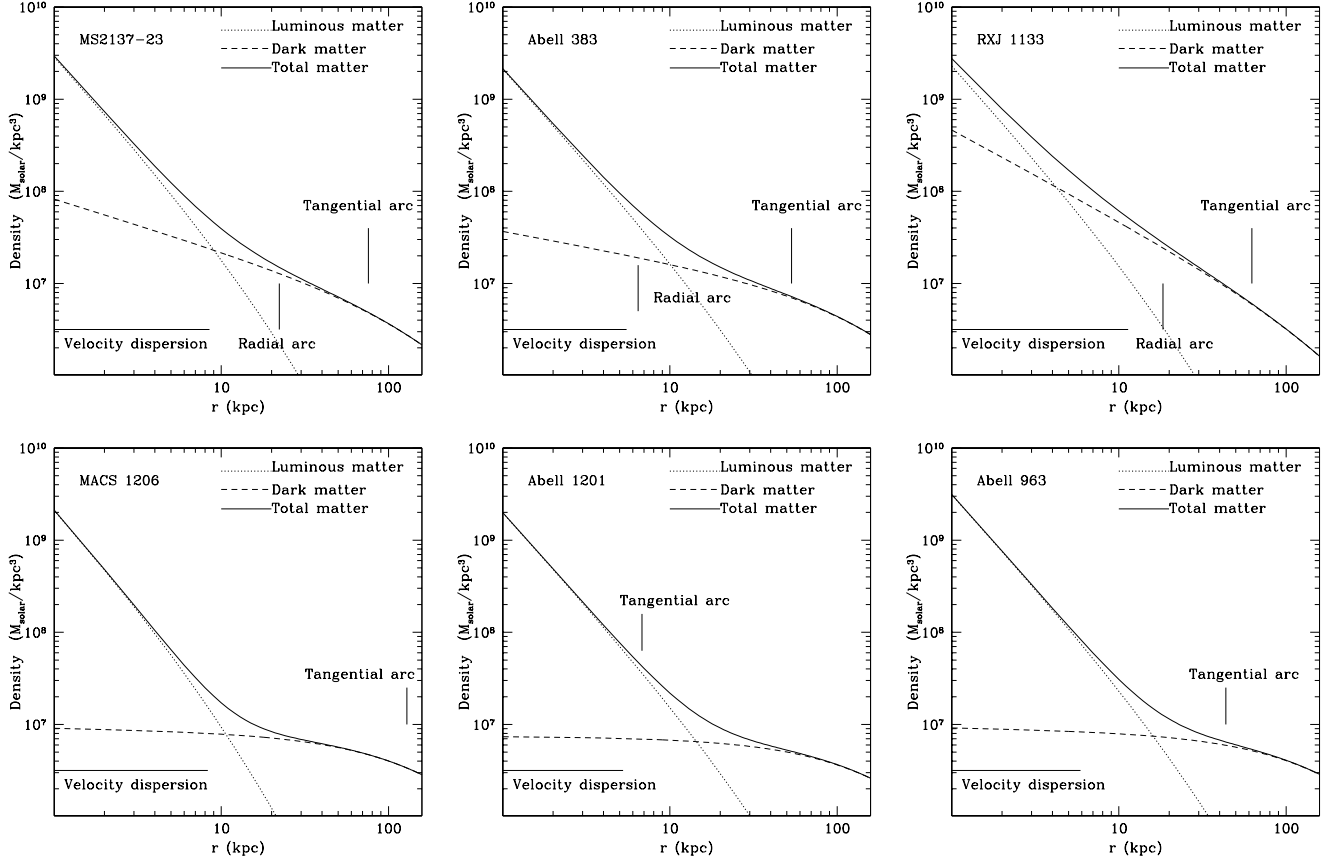


Fig. 8.— Best-fitting total density profile for the entire sample. The positions of the gravitational arcs and the range over which we were able to measure the velocity dispersion profile are noted. Within $\lesssim 10$ kpc the total density distribution is dominated by the BCG.

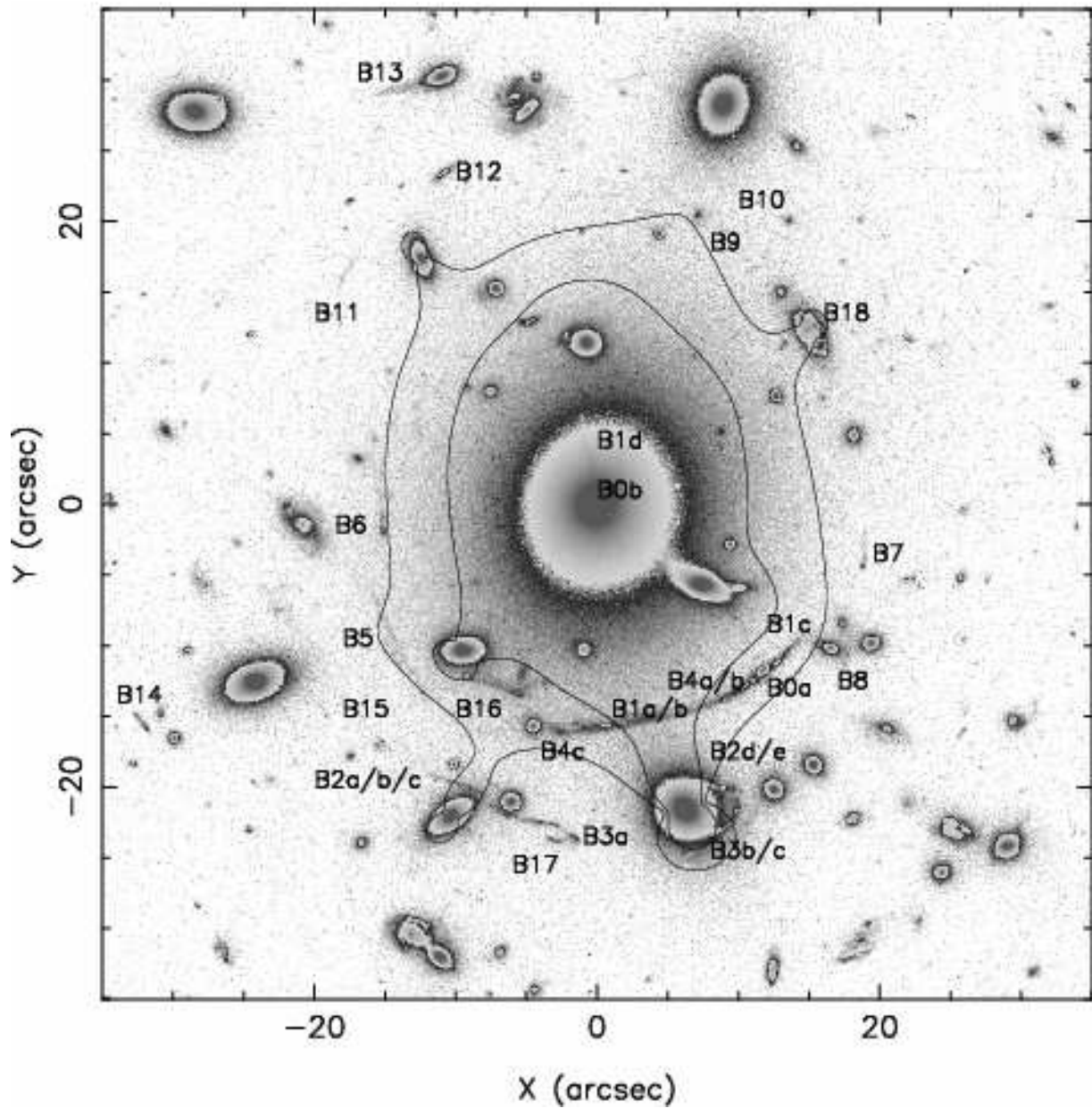


Fig. 9.— The central region of Abell 383 as seen with HST WFPC2. Overlaid are the $z = 1$ and $z = 3$ tangential critical lines calculated from the LENSTOOL analysis using the updated S01 model. The alphanumeric labels are identical to those in Fig. 1 of S01 and identify several of the lensing and cluster galaxy components used to construct the model.

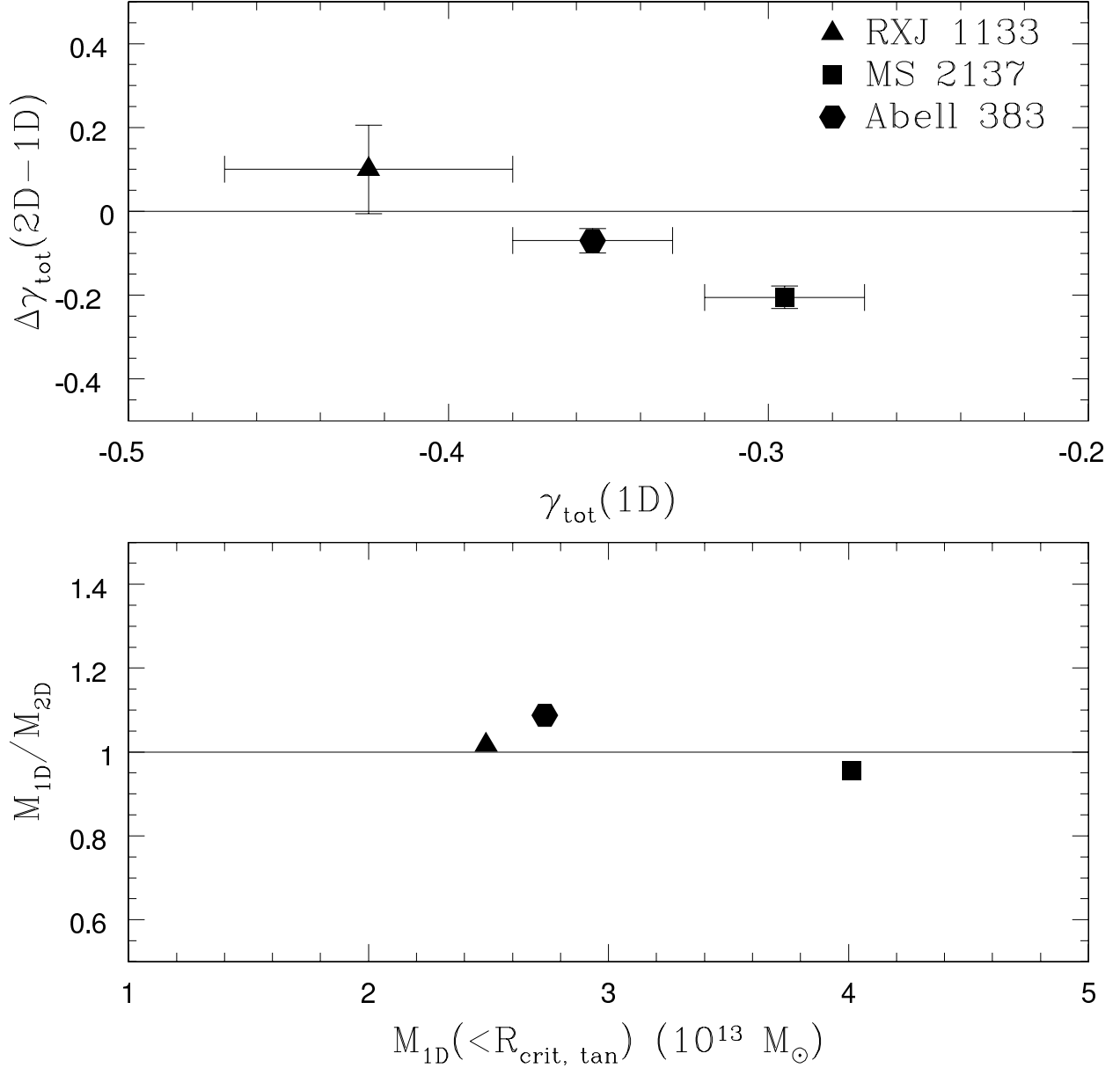


Fig. 10.— Comparison between the 1D models and the 2D check performed with the LENSTOOL software package. We use γ to parameterize the logarithmic slope of the surface density profile. At the radial critical line, γ should be identical for the two methods. (Top panel) The difference in the logarithmic slope between the two methods versus the 1D logarithmic slope. The most discrepant cluster, MS2137-23, would at most effect the DM halo by $\Delta\beta \sim 0.2$ in a direction further away from that predicted by simulations. (Bottom panel) Ratio of the mass enclosed at the tangential critical line, $M(< R = R_{\text{tangential}})$, for the two methods versus the mass enclosed for the 1D method. There are no deviations greater than $\sim 8\%$. The uncertainties in a given data point are approximately the same size as the points themselves.

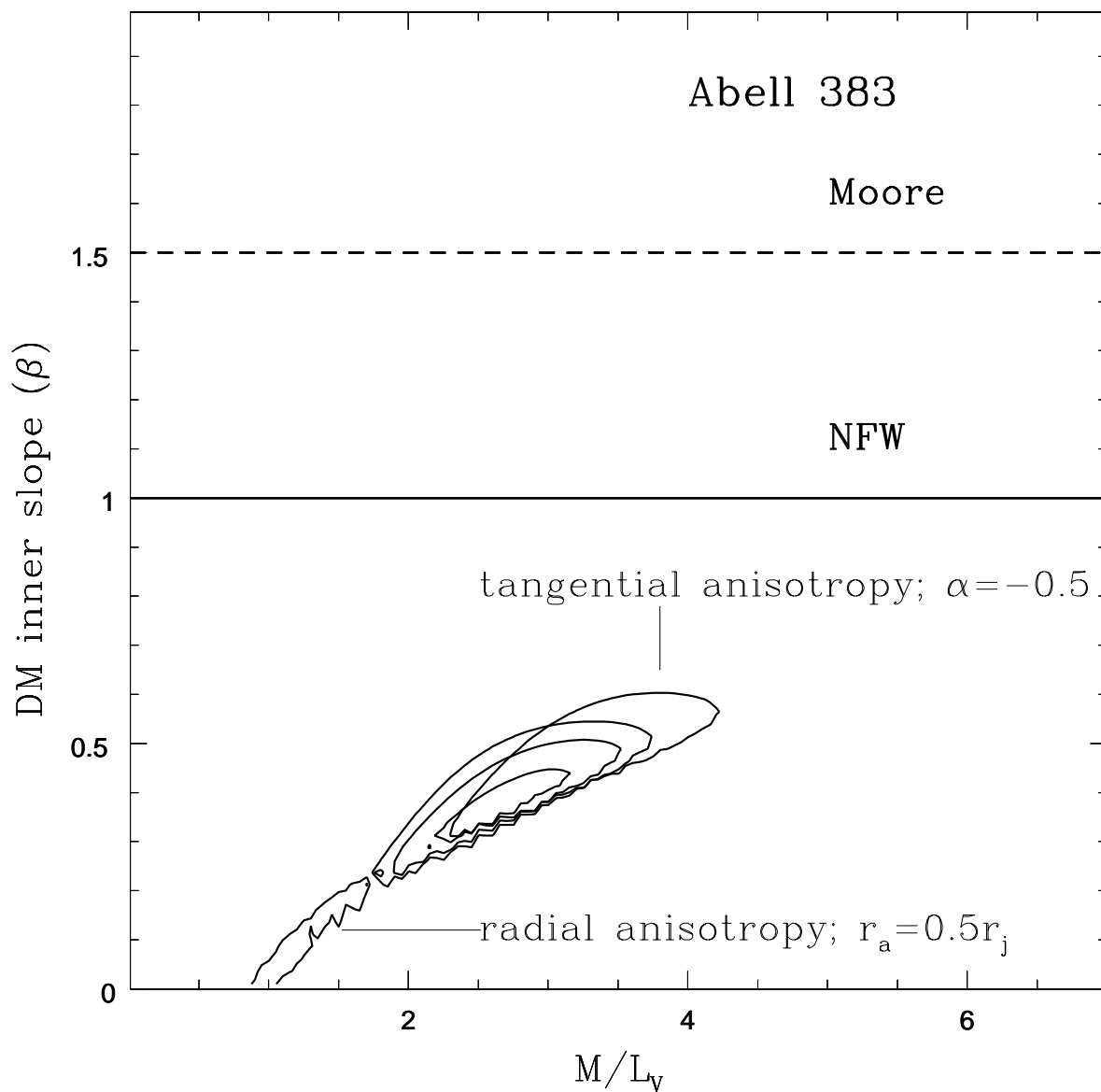


Fig. 11.— The 68%, 95% and 99% confidence contours of Abell 383 along with the 95% confidence contours for the orbital anisotropy tests in § 6.2 that were most discrepant with our original results. No test causes a shift in the β direction greater than $\Delta\beta \sim 0.2$.